Ocean circulation and sea-ice thinning induced by melting ice shelves in the Amundsen Sea

Nicolas C. Jourdain, Pierre Mathiot, Nacho Merino, Gaël Durand, Julien Le Sommer, Paul Spence, Pierre Dutrieux, Gurvan Madec

AGU PUBLICATIONS

JGR

Journal of Geophysical Research: Oceans

RESEARCH ARTICLE

10.1002/2016JC012509

Key Points:
- Amundsen Sea ice-shelves melt induces circulations into/out of ocean cavities, 100–500 times stronger than net meltwater flows
- These circulations bring 4–20 times more heat into cavities than is required for melt
- Ice shelves act as important pumps upwelling heat from deep layers to the surface and decreasing sea-ice volume in their vicinity

Correspondence to:
N. C. Jourdain,
nicolas.jourdain@univ-grenoble-alpes.fr

Citation:
Jourdain, N. C., P. Mathiot, N. Merino, G. Durand, J. Le Sommer, P. Spence, P. Dutrieux, and G. Madec (2017), Ocean circulation and sea-ice thinning induced by melting ice shelves in the Amundsen Sea, *J. Geophys. Res. Oceans*, *122*, 2550–2573, doi:10.1002/2016JC012509.

Received 28 OCT 2016
Accepted 8 FEB 2017
Accepted article online 11 FEB 2017
Published online 30 MAR 2017

Ocean circulation and sea-ice thinning induced by melting ice shelves in the Amundsen Sea

Nicolas C. Jourdain[1], Pierre Mathiot[2], Nacho Merino[1], Gaël Durand[1], Julien Le Sommer[1], Paul Spence[3], Pierre Dutrieux[4], and Gurvan Madec[5,6]

[1]Université Grenoble Alpes, CNRS, IRD, IGE, Grenoble, France, [2]Met Office, Exeter, UK, [3]ARC Centre of Excellence for Climate System Science and Climate Change Research Centre, University of New South Wales, Sydney, New South Wales, Australia, [4]Lamont-Doherty Earth Observatory, Columbia University, New York, New York, USA, [5]Laboratoire d'Océanographie et du Climat: Expérimentation et Approches Numériques, CNRS/IRD/UPMC/MNHN, Paris, France, [6]National Oceanographic Centre, Southampton, UK

Abstract A 1/12° ocean model configuration of the Amundsen Sea sector is developed to better understand the circulation induced by ice-shelf melt and the impacts on the surrounding ocean and sea ice. Eighteen sensitivity experiments to drag and heat exchange coefficients at the ice shelf/ocean interface are performed. The total melt rate simulated in each cavity is function of the thermal Stanton number, and for a given thermal Stanton number, melt is slightly higher for lower values of the drag coefficient. Sub-ice-shelf melt induces a thermohaline circulation that pumps warm circumpolar deep water into the cavity. The related volume flux into a cavity is 100–500 times stronger than the melt volume flux itself. Ice-shelf melt also induces a coastal barotropic current that contributes 45 ± 12% of the total simulated coastal transport. Due to the presence of warm circumpolar deep waters, the melt-induced inflow typically brings 4–20 times more heat into the cavities than the latent heat required for melt. For currently observed melt rates, approximately 6–31% of the heat that enters a cavity with melting potential is actually used to melt ice shelves. For increasing sub-ice-shelf melt rates, the transport in the cavity becomes stronger, and more heat is pumped from the deep layers to the upper part of the cavity then advected toward the ocean surface in front of the ice shelf. Therefore, more ice-shelf melt induces less sea-ice volume near the ice sheet margins.

Plain Language Summary The ice-shelf cavities of the Amundsen Sea, Antarctica, act as very powerful pumps that create strong inflows of warm water under the ice-shelves, as well as significant circulation changes in the entire region. Such warm inflows bring more heat than required to melt ice, so that a large part of that heat exits ice-shelf cavities without being used. Due to mixing between warm deep waters and melt freshwater, melt-induced flows are warm and buoyant when they leave cavities. Therefore, they reach the ocean surface near ice-shelf fronts and can melt significant amounts of sea ice. It is thus suggested that climatic trends in sub ice-shelf melt could partly explain sea ice trends near the ice-sheet margins in the Amundsen Sea region.

1. Introduction

The relative contribution of polar ice sheets to sea level rise has increased since the 1990s [*Shepherd et al.*, 2012]. The observed Antarctic mass loss is explained by acceleration and thinning of a number of glaciers presenting a marine termination, particularly in West Antarctica. For example, ~10% of the global sea level rise over 2005–2010 has been attributed to the glaciers flowing into the Amundsen Sea [*Shepherd et al.*, 2012; *Church et al.*, 2013]. This region has been experiencing rapid grounding line retreats since the 1990s [*Rignot et al.*, 2014], and ice flux through grounding lines have increased by 77% from the 1970s to 2013 [*Mouginot et al.*, 2014]. Such rapid evolution is reminiscent of the concept of marine ice sheet instability (MISI), hypothesized a few decades ago [*Mercer*, 1968, 1978; *Hughes*, 1973] and supported by theory [*Weertman*, 1974; *Schoof*, 2007] and models [*Favier et al.*, 2014; *Joughin et al.*, 2014]. A complete collapse of the West Antarctic ice sheet would increase global sea level by 3.3 m [*Bamber et al.*, 2009]. Ice sheet/glacier simulations indicate that increased melt rates at the ocean/ice-shelf interface can trigger a MISI [*Payne et al.*, 2004], in particular for Pine Island Glacier (PIG) [*Favier et al.*, 2014] and Thwaites Glacier (TWG) [*Joughin et al.*,

2014]. The aforementioned studies are nonetheless based on simple depth-dependent melt formulations, which can lead to large errors in mass loss estimates over 50 year timescales [*De Rydt and Gudmundsson*, 2016]. Obtaining realistic melt rates in an ocean model remains challenging, in particular in the Amundsen Sea region [*Timmermann and Hellmer*, 2013; *Nakayama et al*., 2014b].

The Amundsen Sea embayment presents the strongest basal melt rates in Antarctica [*Depoorter et al*., 2013; *Rignot et al*., 2013], because the deep ice-shelf drafts are exposed to Circumpolar Deep Waters (CDW) that can reach the coast in this region [*Jacobs et al*., 2012]. CDW enter the Amundsen Sea continental shelf at depths greater than 300 m, with temperatures more than 3.5°C above the freezing point [*Jacobs et al*., 2011]. Ice/ocean interactions are complex, and in the relatively small ice-shelf cavities of the Amundsen Sea, only a part of the heat brought by CDW is used to melt ice [*Walker et al*., 2007; *Little et al*., 2009; *Wåhlin et al*., 2010; *Jacobs et al*., 2011; *Ha et al*., 2014]. For example, *Bindschadler et al*. [2011] have estimated that only about 22% of the sensible heat available in CDW is being used to melt ice in Pine Island cavity. The remaining heat is transported to the level of zero buoyancy by melt-induced convection that flows out of the cavity. This is equivalent to a significant melt-induced heat flux at the base of winter surface waters [*Jenkins*, 1999] and may open polynyas in the vicinity of ice-shelf fronts [*Payne et al*., 2007; *Mankoff et al*., 2012]. The influx of CDW toward ice-shelf cavities are influenced by zonal wind variations [*Thoma et al*., 2008; *Dinniman et al*., 2011; *Steig et al*., 2012; *Spence et al*., 2014]. Unlike in other regions around Antarctica, brine-densified winter waters in the Amundsen Sea do not generally penetrate deep into the CDW layer [*Walker et al*., 2007; *Petty et al*., 2014], except in some coastal polynya for particularly strong atmospheric events [*St-Laurent et al*., 2015]. These complex interactions between ice shelves and their environment has motivated the use of regional and global ocean model configurations to estimate melt rates [e.g., *Nakayama et al*., 2014a; *Dinniman et al*., 2015; *St-Laurent et al*., 2015].

In this paper, a new regional configuration of the Amundsen Sea and its ice shelves is presented (section 2) and evaluated with regards to observations (section 3). Beyond model evaluation, this paper brings further insights into the ocean circulation (section 4) and heat transport (section 5) induced by ice-shelf melt. To clearly identify the influence of varying melt rates, we run sensitivity experiments to the drag (C_d) and turbulent heat (salt) transfer coefficients Γ_T (Γ_S) that are all poorly constrained by observations. To our knowledge, the only observational study that attempted to estimate the aforementioned coefficients from observations is indeed by *Jenkins et al*. [2010]. An extended description of the aforementioned coefficients and their estimates is provided in Appendix A. Previous studies analyzed the melt sensitivity to C_d and Γ_T in various models. Their findings are that (i) melt rates increase with increasing C_d [*Walker et al*., 2013; *Dansereau et al*., 2014] and tend to saturate for high C_d values in warm cavities [*Gwyther et al*., 2015]; (ii) the buoyancy effect of higher melt rates overwhelms the dynamical effect of increased roughness, i.e., ocean circulation in a cavity is stronger for higher C_d [*Dansereau et al*., 2014; *Gwyther et al*., 2015], and (iii) for a given C_d, melt rates increase with increasing Γ_T, at a rate that decreases with Γ_T [*Asay-Davis et al*., 2015]. We find similar results in our simulations and further emphasize the primary importance of the thermal Stanton number ($St_T = \sqrt{C_d}\Gamma_T$, see Appendix A) to constrain melt rates (section 4). By varying the drag and transfer coefficients, we actually vary melt rates while keeping physically consistent circulation in ice-shelf cavities. This enables the quantification of melt-induced ocean circulation and heat transport within the ice-shelf cavities and in their vicinity.

2. Material and Methods

2.1. Ocean/Sea-Ice Model

We make use of NEMO-3.6 (Nucleus for European Modelling of the Ocean) [*Madec and NEMO-team*, 2016] that includes the ocean model OPA (Océan Parallélisé) and the Louvain-la-Neuve sea-ice model LIM-3.6 [*Rousset et al*., 2015], here used with only one ice category. Our model settings include a 55-term polynomial approximation of the reference Thermodynamic Equation Of Seawater (TEOS-10) [*IOC, SCOR, IAPSO*, 2010] optimized for a Boussinesq fluid [*Roquet et al*., 2015], a split-explicit free surface formulation, a flux-corrected transport scheme for tracers advection [*Lévy et al*., 2001], a vector-form formulation for momentum advection, and nonlinear bottom friction with the same parameter values as *Treguier* [1992]. We use Laplacian isoneutral diffusion and bi-Laplacian horizontal viscosity with the same coefficient values as *Treguier et al*. [2014]. Vertical mixing coefficients are calculated through a TKE scheme and convection is

Table 1. Model Parameters Used in the NEMO Ice-Shelf Module[a]

Parameter	Value	Description
g	9.80665 m s^{-2}	Gravity parameter
ρ_w	1026.000 kg m^{-3}	Reference seawater density
ρ_i	920.000 kg m^{-3}	Reference ice-shelf density
L_f	334.000 kJ kg^{-1}	Latent heat of fusion of ice
c_{pw}	3991.868 J kg^{-1} K^{-1}	Seawater heat capacity
c_{pi}	2000.000 J kg^{-1} K^{-1}	Ice-shelf heat capacity
T_{si}	−20°C	Ice-shelf temperature at sea level
κ_i	1.54×10^{-6} m^2 s^{-1}	Ice-shelf thermal diffusivity
λ_1	−0.0564°C/(g kg^{-1})	Liquidus slope (for cons. temp. and abs. sal.)
λ_2	0.0773°C	Liquidus intercept (for cons. temp)
λ_3	-7.8633×10^{-4}°C db^{-1}	Liquidus pressure coef. (for cons. temp)
C_d	1.00×10^{-3}	Default top drag coef.
Γ_T	2.21×10^{-2}	Default heat exchange coef. (St_T = 0.0007)
Γ_S	6.19×10^{-4}	Default salt exchange coef.

[a]The λ_k coefficients are calculated from a least-mean-square linear regression of the conservative temperature at which seawater freezes [*IOC, SCOR, IAPSO*, 2010] in the 200–1200 db and 15–35 g kg^{-1} ranges for pressure and absolute salinity, respectively.

parameterized through enhanced mixing coefficients in case of static instability (same coefficients as *Treguier et al.* [2014]).

Our model setup also includes the new ice-shelf module that was developed by P. Mathiot et al. (Different ways to represent ice shelf melting in a z* coordinate ocean model, unpublished manuscript, 2017). From a dynamical point of view, ice shelves affect the horizontal pressure gradient through the hydrostatic pressure exerted by ice on the ocean column and create a friction at the top of the water column. As for bottom cells, the top cell thickness is adjusted to follow the actual ice-draft, with an approach similar to the partial cells used by *Barnier et al.* [2006]. Meltwater is treated as a volume flux, i.e., it affects the ocean flow divergence near the ice draft. It is important to note that the ice shelf is static, so it is implicitly assumed that ice dynamics instantaneously compensates melt-induced thinning. Freshwater and heat exchanges at the ice/ocean interface are analytically derived from three equations that represent (1) heat balance at the interface accounting for phase change, turbulent exchange in water, and diffusion in the ice; (2) salt balance accounting for freezing/melting and turbulent exchange; and (3) pressure and salinity dependence of the conservative temperature at which seawater freezes [*Hellmer and Olbers*, 1989; *Holland and Jenkins*, 1999; *Losch*, 2008; *Jenkins et al.*, 2010]

$$\rho_i m L_f + \rho_w c_{pw} \sqrt{C_d} u_{TML} \Gamma_T (T_b - T_{TML}) + \rho_i c_{pi} \kappa_i (T_b - T_{si})/D_b = 0, \quad (1)$$

$$\rho_i m S_b + \rho_w \sqrt{C_d} u_{TML} \Gamma_S (S_b - S_{TML}) = 0, \quad (2)$$

$$T_b = \lambda_1 S_b + \lambda_2 + \lambda_3 \rho_w g D_b, \quad (3)$$

where $\rho_i m$ is the melt rate in kg m^{-2} s^{-1}, T_b and S_b the conservative temperature and absolute salinity along the ice-shelf base (at depth D_b), T_{TML}, S_{TML}, and u_{TML} the conservative temperature, absolute salinity, and velocity averaged over the top mixed layer (TML) that we define as a 30 m layer at the top of the cavity (or the entire top level where top levels are thicker than 30 m), and the other parameters are described in Table 1. More details on the second term in (1) are provided in Appendix A.

2.2. The AMU12.L75 Model Configuration

We use a regional NEMO configuration that is hereafter referred to as AMU12.L75. It is an extraction of the global ORCA12 Mercator grid [e.g., *Treguier et al.*, 2014] centered on the Amundsen Sea (Figure 1). The resolution is isotropic and equals 1/12° in longitude, which typically corresponds to 2.4 km under Pine Island ice shelf, ~3 km along the continental shelf break, and 4.2 km along the northern domain boundary. Such resolution is sufficient to partially resolve mesoscale eddies in the deep Southern Ocean [*Hallberg*, 2013] and the mean flow-topography interactions involved in the CDW transport onto the continental shelf [*St-Laurent et al.*, 2013; *Assmann et al.*, 2013; *Nakayama et al.*, 2014b], but not to resolve heat transport by eddies and Rossby wave-topography interactions on the continental shelf [*Stewart and Thompson*, 2015; *St-Laurent et al.*, 2013]. As commonly practiced in the Drakkar and European CMIP communities, there are 75 vertical levels with thickness increasing from 1 m at the ocean surface to 204 m at 6000 m (via thicknesses of 54 m at 510 m and 95 m at 947 m). The bathymetry and ice-shelf draft are interpolated from BEDMAP2 [*Fretwell et al.*, 2013] onto the model grid, with a smooth transition along the lateral boundaries to match the bathymetry of the simulation used as lateral boundary conditions.

The lateral boundary conditions (sea-ice fraction and thickness, ocean salinity, temperature, and velocities) are taken from 5 day outputs of the global 0.25° simulation produced by *Spence et al.* [2014] and spun up

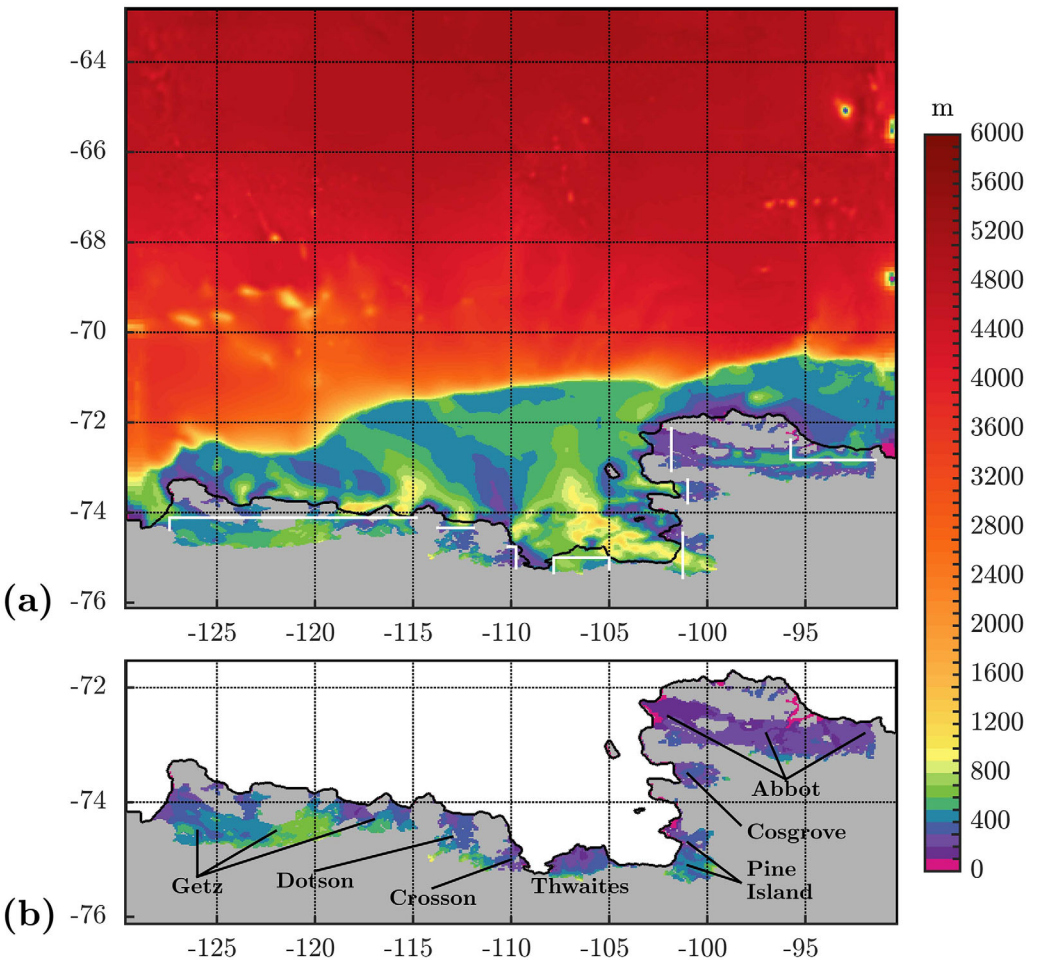

Figure 1. (a) Bathymetry of the model domain. (b) Depth of the ice-shelf drafts. Grounded ice is shaded in gray, and black contours indicate the ice sheet front. The white lines in Figure 1a indicate the sections used to calculate the overturning circulation in Figure 7.

for 100 years. Consistently with *Spence et al*. [2014], atmosphere surface boundary conditions are derived from version 2 of the Coordinated Ocean-ice Reference Experiments (CORE-2) Normal Year Forcing (NYF) [*Griffies et al*., 2009; *Large and Yeager*, 2009] and applied through the CORE bulk formulae. Sea surface salinity (SSS) is also relaxed toward Spence's SSS (with a piston velocity of 50 m for 300 days as in *Treguier et al*. [2014]), but only further than 200 km from the coast in order not to overly constrain freshwater exchanges near coastal polynya, ice-shelf fronts, and icebergs. The climatological monthly iceberg runoff produced by *Merino et al*. [2016b] is prescribed in our simulations (87% of this iceberg meltwater is released within 200 km from the coast in this region). The later accounts for meltwater released by drifting icebergs and is based on observational calving flux estimates. Penetration of solar radiation in the visible spectrum is prescribed through a three-waveband scheme [*Lengaigne et al*., 2009] that depends on the climatological seasonal chlorophyll-A concentrations from the SeaWIFS data set [*O'Reilly et al*., 1998].

2.3. Simulations

In order to assess the model performance with regards to the available observations, we run a 20 year reference experiment, hereafter referred to as AMU12.L75-REF, that is carried out with C_d=0.0010 and Γ_T=0.022. Such values were chosen empirically, within the literature range, and in a way that limits biases for Thwaites and Pine Island (see section 3). The corresponding St_T value (see definitions in Appendix A) is 0.0007, which is slightly lower than the 0.0011–0.0016 range suggested by *Jenkins et al*. [2010] based on measurements under an ice shelf and on previous results from studies about sea ice in contact with above-freezing water. The model spin-up is mostly achieved after approximately 3 years (Figure 2). The relative seasonal cycle is nonnegligible, but relatively small for Getz, Thwaites, and Pine Island, with an amplitude

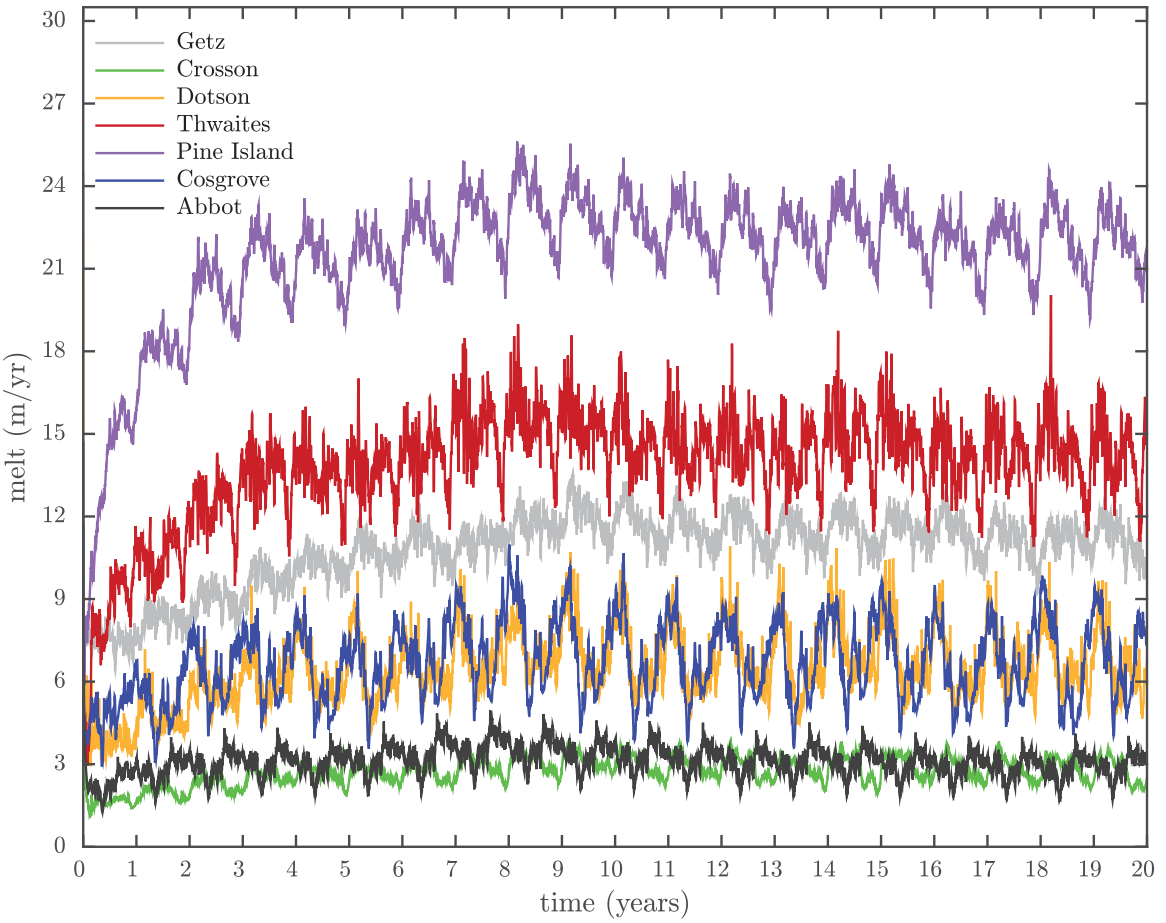

Figure 2. Mean melt rates in the simulated cavities.

representing 14, 21, and 13% of the annual mean, respectively (calculated from 10 year monthly averages). It is relatively larger for the other ice-shelf cavities where its amplitude represents 35–58% of the annual mean. Intrinsic variability, i.e., interannual variability that would appear despite a normal year forcing, is small. All the model diagnostics presented in section 3 are based on averages over the last 10 years of the reference experiment. In sections 4 and 5, we use 17 other simulations that only differ from the reference experiment by the C_d and Γ_T values. One of these simulations is with no melt (Γ_T=0), while the 16 others correspond to four groups, each of them consisting of four simulations of same thermal Stanton number but different (C_d,Γ_T) combinations. *McPhee* [2008] argued that the Γ_T to Γ_S ratio is between 35 and 70. For simplicity, this ratio is set to 35 in all our simulations. As the spin-up is quite short, the fifth year of the 18 experiments is used in sensitivity analyses in order to limit the computational cost. All the plots and estimates provided in sections 4 and 5 are essentially unchanged when the fourth year is used instead (not shown).

2.4. Observational Data Sets

To evaluate the simulated sea-ice cover, we use the 1979-2013 NOAA/NSIDC Climate Data Record (CDR) of sea-ice concentration from passive microwave data, version 2 [*Meier et al*., 2013]. The evaluation of simulated temperature is based on 1140 CTD (Conductivity-Temperature-Depth) profiles collected during summer campaigns over 1994–2014 [*Dutrieux et al*., 2014]. The comparison to CTDs is done by sampling our model outputs in space and time of the year following the actual CTD distribution. We also use the transport budgets based on observations in front of Pine Island and reported in *Dutrieux et al*. [2014], and we have recalculated the heat budgets from these data following the published methodology. Finally, our assessment of total ice-shelf melt is based on estimates obtained for individual ice shelves by *Depoorter et al*. [2013] and

Rignot et al. [2013] through input/output methods (based on surface mass balance modeling and glaciological satellite observations). These estimates are representative of the late 2000s.

3. Evaluation of the Reference Simulation

This section consists of a brief evaluation of the reference experiment AMU12.L75-REF. The latter is constrained by CORE-2-NYF, which was built from complex treatment of reanalysis data over 1958–2010 [*Large and Yeager*, 2004] and does not present any interannual variability. In the following, we compare model outputs to available observational products that are more recent and present significant interannual variability. Therefore, differences between model and observations do not only reflect intrinsic biases in NEMO but can also reflect interannual variability and climate trends.

First, we evaluate sea-ice cover because it gives an integrated assessment of the simulation, gives access to the seasonal cycle (in situ measurements in winter are extremely rare), and is related to the ocean stratification. The simulated sea-ice extent is underestimated in summer and overestimated in winter compared to the NSIDC climatology, and the simulated seasonal cycle lays just within the observed interannual extrema (Figure 3). An overestimated amplitude of the sea-ice seasonal cycle in the Amundsen Sea is found in the global *Spence et al*. [2014] simulation used to constrain AMU12.L75 (Figure 3), as well as in a majority of global ocean models forced by the interannual version of CORE-2 [*Downes et al*., 2015]. Similar biases are also present in global NEMO simulations under the Drakkar Forcing Set which is based on ERA reanalyses (B. Barnier, personal communication), so that these biases are likely related to deficiencies in (elasto-)viscoplastic sea-ice models.

Then, we compare summer temperature profiles to CTD measurements (Figures 4b–4g). There is a large overlap between the observed and simulated interpercentiles shaded area over 100–500 m for all locations in the vicinity of ice shelves (Figures 4b, 4c, 4d, and 4f). Nonetheless, the mean summer thermocline simulated at all locations is shallower than the observational mean, and mean temperatures over 100–500 m are 0.8–1.7°C warmer than observed. Even though several kinds of model biases can lead to such warm bias, the later could be partly related to the overestimated sea-ice seasonal cycle in the model, because forming

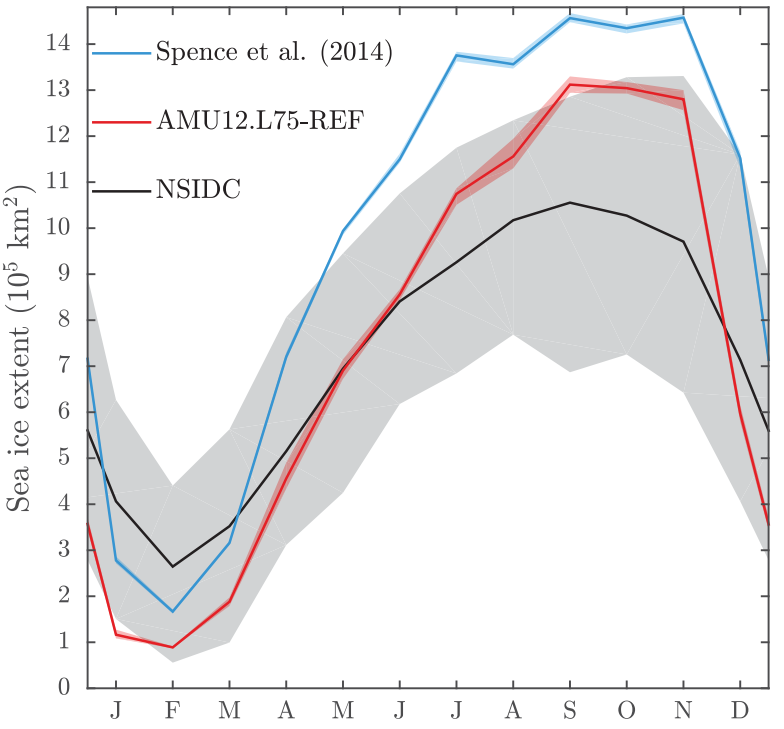

Figure 3. Climatological sea-ice extent (i.e., area where monthly sea-ice concentration is greater than 15%) between 95°W and 125°W in NSIDC's climate data record (gray), in AMU12.L75-REF (red), and in the simulation from *Spence et al*. [2014] (blue). Shaded areas indicate the interannual minima and maxima.

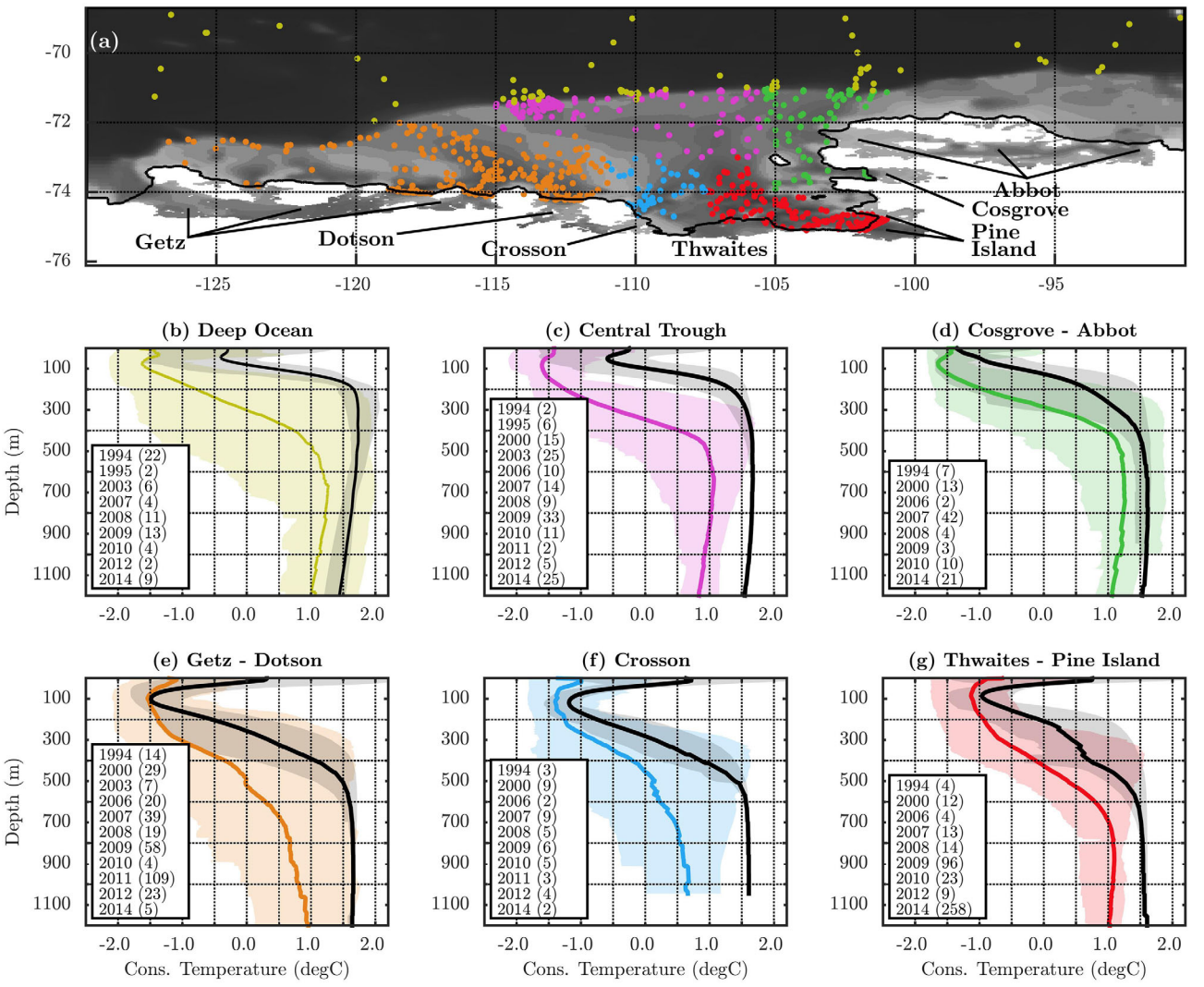

Figure 4. (a) Location of the CTD profiles used in this paper, each color indicating a different region. (b–g) Observed mean temperature profile over all CTD profiles (solid color lines), outputs from the reference experiment sampled in space and time of the year as the CTD profiles (solid black). The shaded areas in Figures 4b–4g represent the 5þ and 95þ percentiles. The number of CTD profiles for each year (November–December measurements being counted together with the next year's summer months) is indicated for each region.

more sea ice in winter and melting this excess in summer is expected to result in a shallower surface layer, i.e., a more stratified thermocline. Between 500 and 1000 m, where stronger ice-shelf melt rates are found, temperatures are approximately 0.5°C warmer than the observational mean near Abbot, Cosgrove, Pine Island, and Thwaites (Figures 4b and 4d), and 1.1°C warmer than the observational mean near Getz, Dotson, and Crosson (Figures 4c and 4f). Simulated profiles at depth are slightly above the observational interpercentiles range, indicating a bias. Given that CDW in the Amundsen Sea is typically 3.5°C above the freezing point, a warm bias of 0.5°C would typically lead to an overestimation of melt rates by 15% according to (1). In other words, realistic melt rates can be obtained despite the warm bias with a Stanton number 15% lower than it should be.

We now assess simulated melt rates compared to the observation-based estimates by *Depoorter et al.* [2013] and *Rignot et al.* [2013]. It is important to note that the two observational ranges of uncertainty do not overlap for all the cavities (Figure 5), indicating that the actual uncertainty may be larger than reported in these papers. The simulated total melt rate is within the observational range of uncertainty for Thwaites and Abbot and is slightly overestimated for Pine Island and Cosgrove (by 9 and 15%, respectively). Biases are larger for Dotson and Crosson, where total melt rates are underestimated by 24 and 71%, respectively, and for Getz where total melt rate is overestimated by 72%. A part of these biases in melt rates are likely

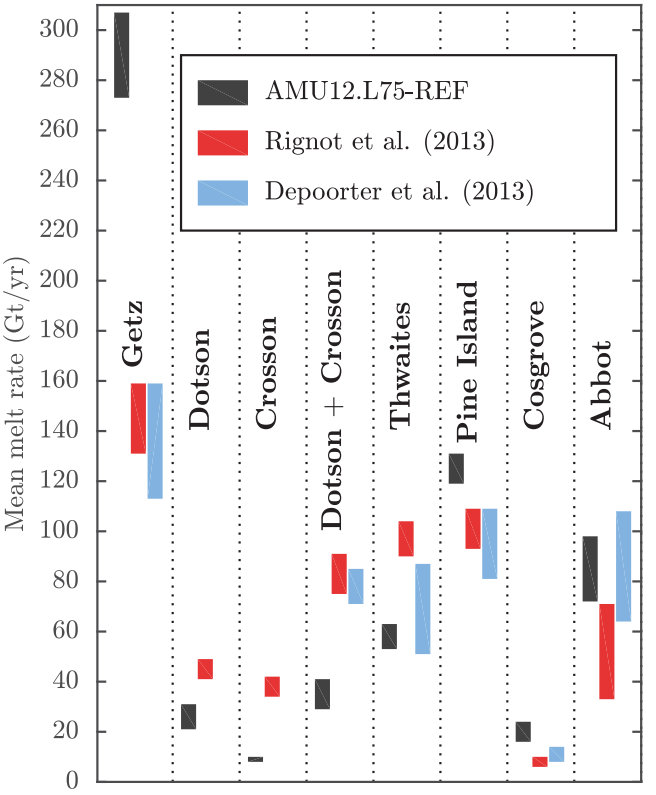

Figure 5. Total melt rates simulated in AMU12.L75-REF, compared to observational estimates by *Rignot et al*. [2013] and *Depoorter et al*. [2013]. The range of uncertainty related to AMU12.L75-REF is calculated as one standard deviation of the daily time series.

related to the poor representation of the Amundsen Sea topography in BEDMAP2, in particular for Getz [*Schaffer et al*., 2016]. The underestimated melt rate in Dotson cavity could be related to the effects of tides that are stronger for Dotson than for Getz and Pine Island [*Robertson*, 2013] but that are not included in our configuration. Overall, the aforementioned warm bias at the depth of grounding lines is likely compensated by the rather small St_T number used in the reference experiment, so that melt is not overestimated all over the domain. As shown in Appendix B, the melt rate biases are of similar magnitude to those found in other state-of-the-art regional modeling studies. Overall, despite further possible improvements, in particular in terms of sea-ice seasonality and melt rates in Crosson and Getz cavities, we conclude that our simulations are suitable to conduct sensitivity analyses that can be interpreted in a realistic context.

4. Melt-Induced Circulation

First, we analyze the model sensitivity to exchange parameters at the ocean/ice-shelf interface, using the fifth year of 18 simulations that only differ by their (C_d,Γ_T) values. The corresponding melt rates are shown for PIG and TWG in Figures 6a and 6b. As expected, melt rates for a given C_d increase with increasing Γ_T. In first approximation, isomelt lines in Figures 6a and 6b are close to iso-St_T lines. Looking in more details, melt rates along an iso-St_T line slightly decrease with increasing C_d, which is due to weaker ocean velocities in the top mixed layer (not shown). From a modeling perspective, Figures 6a and 6b show that several values of (C_d,Γ_T) can provide a good match between simulated and observed melt, but for Pine Island and Thwaites, St_T should be in the 0.0005–0.0016 range. This range is likely model-dependent. It is also interesting to note that vertical melt distributions (Figures 6c and 6d) are slightly shifted toward deeper parts of the ice draft for simulations with stronger total melt (Figures 6c and 6d).

We now describe the melt-induced ocean circulation within the cavities. Both the overturning and the barotropic components of the circulation within a cavity increase linearly with the total melt rate in that cavity (Figures 7a and 7b). There is no overturning circulation for zero melt rates (see intercept in Figure 7a) because the overturning is driven by the buoyancy of fresh meltwater. By contrast, there is a background barotropic circulation that represents a large part of the total circulation for some cavities like Dotson, but that is much smaller than the melt-induced circulation for other cavities like Cosgrove (see intercept in Figure 7b). The background circulation might either be forced by winds or air-sea buoyancy fluxes or inherited from the initial state. The melt-induced barotropic circulation can be understood as a geostrophic adjustment to stronger horizontal pressure/density gradients in presence of stronger melt [*Jenkins*, 2016]. It can also be understood in terms of potential vorticity conservation which indicates that a stronger meltwater flux induces a stronger vortex stretching, and therefore a source of cyclonic vorticity.

In order to examine budgets for individual cavities, we now consider the total volume transport into the cavity through the ice-shelf front, which also increases linearly with total melt (Figure 7c). This transport compares favorably with observational estimates for Pine Island (empty stars in Figure 7c). A useful metric is

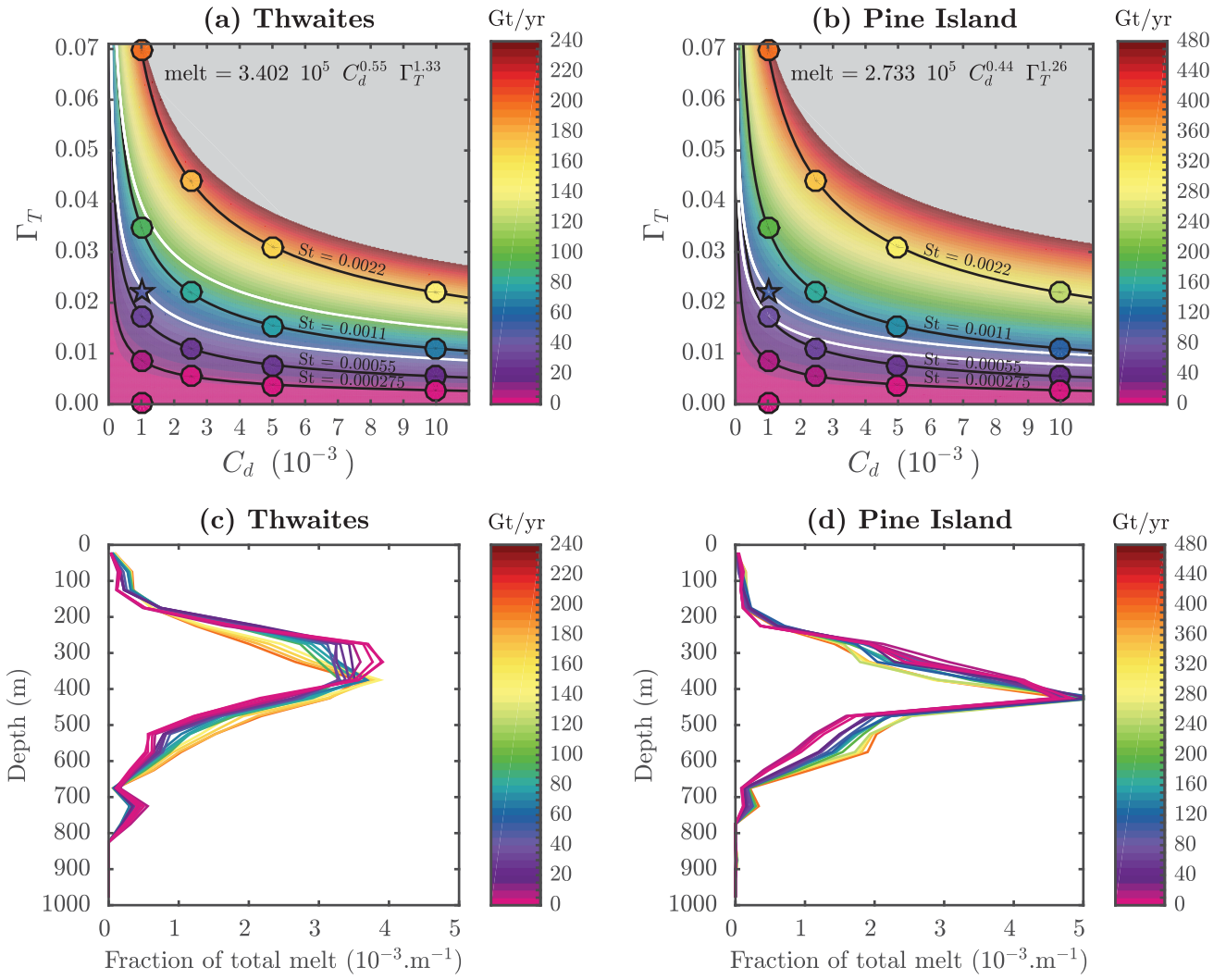

Figure 6. Total melt rate underneath (a) Pine Island glacier and (b) Thwaites glacier as a function of (C_d,Γ_T). Each circle (star for the reference experiment) represents the average over the 5þ year of a simulation. Isolines of same thermal Stanton number are indicated in black. The background colors show the regression of melt rates on powers of C_d and Γ_T (regression coefficients indicated on the plot), with gray shading where interpolated values would exceed the simulation range by more than 20%. The range of observed values (from the input/output methods of *Depoorter et al.* [2013] and *Rignot et al.* [2013], accounting for their uncertainties) is indicated in white (based on the regression values). The lower panels represent the fraction of total melt per depth, i.e., the melt profile normalized by the total melt, for (c) Thwaites and (d) Pine Island. The color used for each profile indicates the associated total melt in the cavity.

the "efficiency of the dynamical pump" (or, in short, dynamical efficiency), η_{dyn}, that we define as the change in total transport into the cavity (in mSv) for a change of 1 mSv in melt volume flux. The term "dynamical pump" refers to the melt-induced circulation, it is related to the term "ice-pump," introduced by *Lewis and Perkin* [1986], that can be misleading in the Amundsen Sea because there is no significant refreezing of meltwater. The dynamical pump is also broader than the Ekman pumping along ice-shelf slopes [*Jenkins*, 2016] in the sense that our definition includes both the Ekman and geostrophic transports. The efficiency of the dynamical pump is typically between 100 and 500 in the cavities of the Amundsen Sea (Figure 7c), meaning that 1 mSv of additional melt (equivalent to ~32 Gt yr^{-1}) will lead to an additional flow of 100–500 mSv into a given cavity. Thus, the melt-induced circulation within an ice-shelf cavity is not mainly driven by mass imbalance due to meltwater buoyancy, but rather by a much stronger circulation. Previous studies have described buoyancy-driven flows where the circulation induced by potential vorticity conservation is stronger than the circulation induced by mass conservation (for the Mediterranean dense overflow [*Özgökmen et al.*, 2001] and for a hydrothermal plume [*Stommel*, 1982]). As described in Appendix C, the melt-induced overturning circulation can also be understood in terms of potential energy budget. The very simple model developed in this Appendix proposes an analytical expression for the dynamical pump efficiency

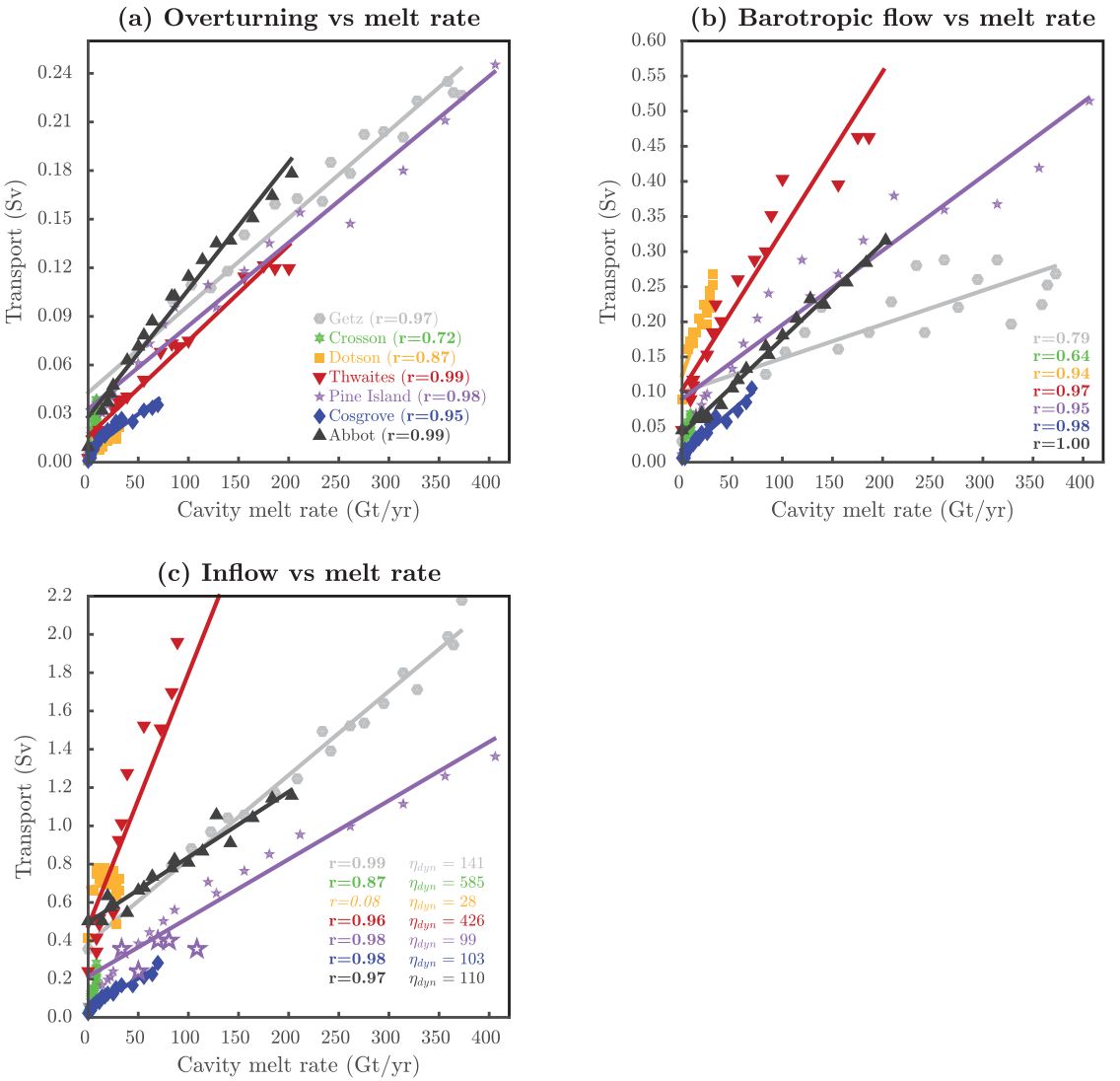

Figure 7. (a) Amplitude of the overturning circulation versus melt in each cavity across the 18 simulations with varying (C_d,Γ_T) values. The overturning circulation is estimated through the sections indicated in white in Figure 1, and calculated as the along-z maximum of $|\int_{z_b}^{z}\int u.dx.dz|$ where z_b is the bottom depth, u the ocean velocity perpendicular to the section, and x the direction along the section. (b) Same as Figure 7a but for the amplitude of the barotropic transport within each cavity, which is calculated as the maximum amplitude (maximum minus minimum) of the barotropic stream function (BSF) under the ice-shelf. (c) Positive seawater transport through the ice-shelf front (positive into the cavity) calculated from daily velocities then averaged over year 5. The lines are least-mean-square regressions, and corresponding correlations (r) are indicated on the lower-right corner (all of them with statistical significance greater than 99%). In Figure 7c, η_{dyn} represents the dynamical efficiency, i.e., the slope expressed in Sv/Sv (see Appendix C for more details on η_{dyn}), and the empty stars correspond to the observational estimates by *Dutrieux et al.* [2014].

and indicates its dependency on cavity geometry and ocean density profile. Basically, the dynamical pump is very efficient ($\eta_{dyn} \gg 1$) for dense CDW and deep grounding lines, and poorly efficient ($\eta_{dyn} \simeq 1$) if the water entering the deepest part of the cavity has a density close to the meltwater density. The presence of relatively dense water near the upper part of the cavity also tends to increase the dynamical efficiency. It should be noted that density variations in polar regions, and therefore η_{dyn}, are mostly controlled by salinity.

Melt-induced circulation is not restricted to ice-shelf cavities; it also concerns the ocean in their vicinity. Here we only describe the response of the westward coastal current (along the ice sheet margins) that is distinct from the westward jet along the continental shelf which is associated with the Antarctic slope front [*Heywood et al.*, 1998]. A tight linear relationship is found between the barotropic transport by the coastal current and the total melt rate in the domain (Figure 8). Assuming that the simulated barotropic circulation is realistic in the range of observed melt rates, we estimate that 45 $\pm$ 12% of the coastal barotropic circulation in the Eastern Amundsen Sea is explained by melt in ice-shelf cavities (compare value in the gray zone to intercept

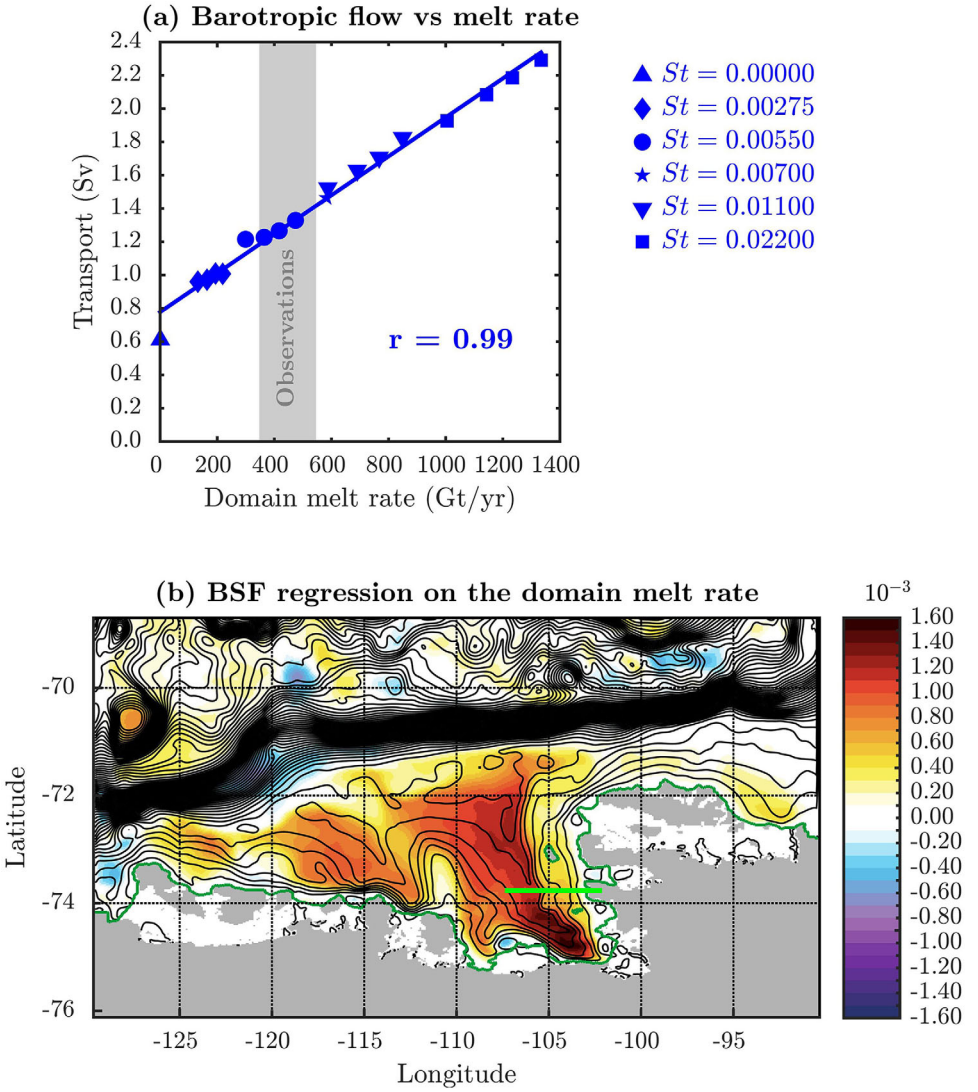

Figure 8. (a) Barotropic transport in the coastal current versus total melt in the simulated ice-shelf cavities, in 18 simulations with varying (C_d,Γ_T) values. The transport is estimated in the Eastern Amundsen Sea at 73.765°S (see light green straight line in Figure 8b), as the barotropic stream function (BSF) difference between the coastline and the first BSF maximum westward. Simulations of identical thermal Stanton number (St_T) are displayed with the same symbol. The line indicates the least-mean-square regression, with corresponding correlation (r) indicated on the plot. The range of observed melt rates is indicated in gray. (b) Regression coefficient (shaded) of the local barotropic stream function on the total melt rate underneath all the ice shelves (units are mSv per Gt yr^{-1}). The black lines are isocontours of the mean barotropic stream function in the AMU12.L75-REF experiment, showing the westward coastal current (along the ice sheet margins) and the westward jet along the continental shelf break and associated with the Antarctic slope front. The dark green contour indicates the ice sheet margin, and gray shading corresponds to grounded ice.

in Figure 8a). Similarly, a 50% increase in melt rates (from present-day value) would typically increase the barotropic transport associated with the coastal current by 24 ± 7%. Similar ratios and very high correlations are found all along the Amundsen Sea coast. These results emphasize the need for realistic meltwater fluxes to study exchanges between the deep ocean and the continental shelf, and between two adjacent basins. For example, the freshwater transport from the Amundsen Sea to the Ross Sea increases with ice-shelf melt in the Amundsen Sea both due to increased meltwater flux and to stronger westward current [*Nakayama et al.*, 2014a].

5. Melt-Induced Heat Transport and Sea-Ice Thinning

We now quantify the heat budget of individual cavities for different melt rates and associated ocean circulation. Details on the heat budget calculation are given in Appendix D. Over a year in steady state, the heat budget can be simplified as

Table 2. Values of the Heat Budget Terms (See Equation (4)) in the Reference Experiment

	H_{IN} (TW)	H_{OUT} (TW)	H_{LAT} (TW)	δ_{th} (%)
Getz	9.71	−6.92	2.77	29
Dotson	3.19	−2.92	0.26	8
Crosson	0.65	−0.58	0.08	11
Thwaites	10.03	−9.45	0.58	6
Pine Island	6.88	−5.59	1.26	19
Cosgrove	0.78	−0.58	0.20	26
Abbot	2.92	−2.01	0.89	31

$$H_{IN} + H_{OUT} = H_{LAT}, \quad (4)$$

where H_{IN} (H_{OUT}) is the heat flux entering (leaving) a given cavity with melting potential, i.e., reference temperature is the surface freezing point because any heat entering the cavity will potentially be transported by the buoyant and rotating flow along the ice draft and melt some ice at upper levels. The heat flux into the cavity (H_{IN}) is partly used to melt ice (H_{LAT}), and the remaining heat flows out of the cavity (H_{OUT}).

The values of the heat budget terms in the reference simulation are displayed in Table 2. Melt rates in individual cavities represent typically 0.1–1 TW, a power equivalent to 0.07–0.7% of the mean global ocean warming over 1955–2010 (based on the estimates by *Levitus et al.* [2012] for the upper 2000 m). The simulated heat inflow into Pine Island cavity is close to the observational estimates (see empty stars in Figure 9a).

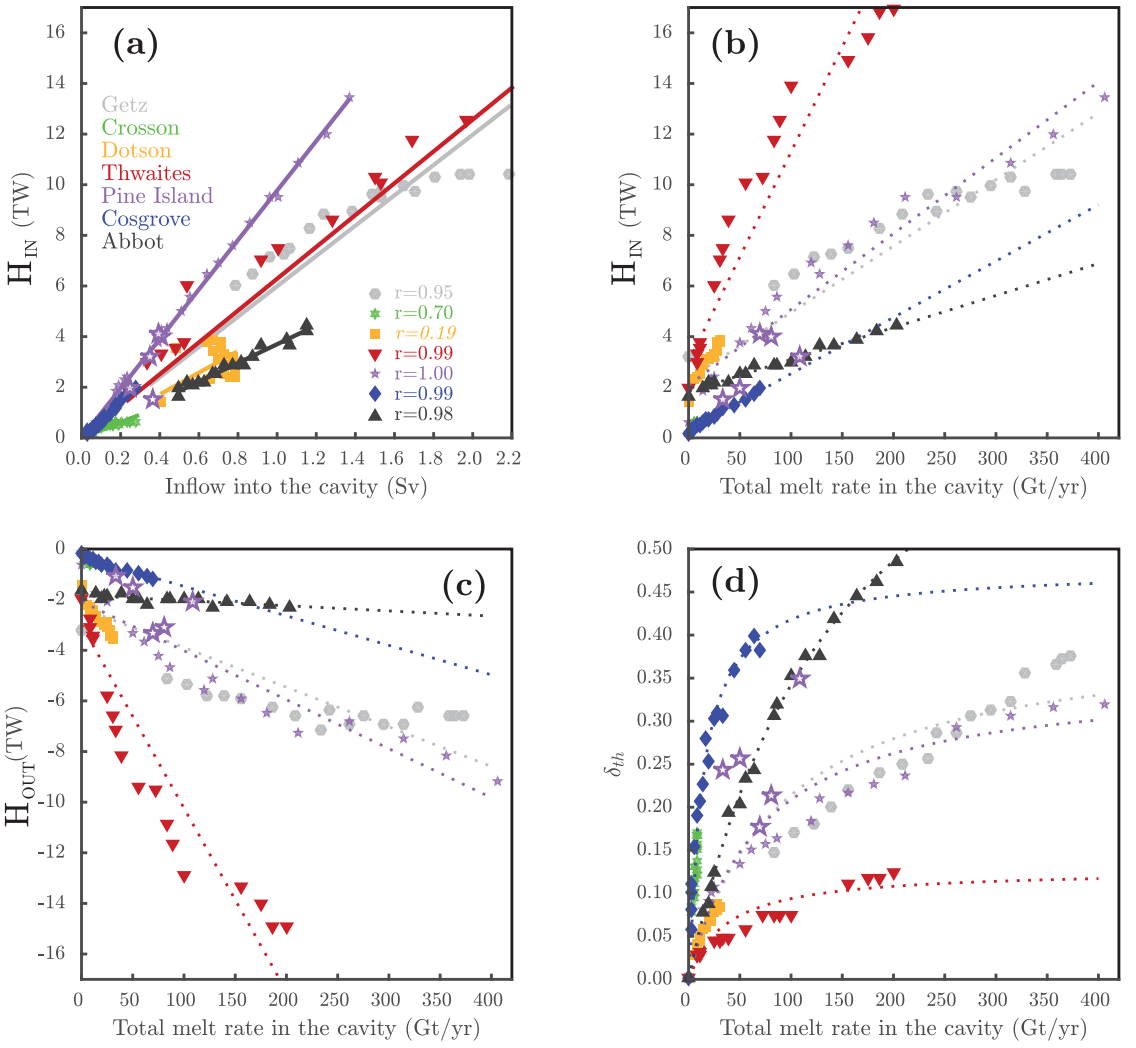

Figure 9. (a) Heat inflow (H_{IN}) versus volume transport (Φ_{IN}) through the ice-shelf front; the lines indicate least-mean-square regressions of the form $H_{IN} = \langle TF \rangle$ TRSP. Figures 9b–9d, respectively, show the heat inflow (H_{IN}), the heat outflow (H_{OUT}), and the thermal efficiency (δ_{th}) versus total melt rate in each cavity. The empty stars show the observational estimates from *Dutrieux et al.* [2014]. The dashed lines in Figures 9b–9d are derived from (D5) in Appendix D, with $\langle TF \rangle$ deduced from the linear fit in Figure 9a of this figure, and η_{dyn} deduced from the linear fit in Figure 7c.

As mentioned in section 1, only a part of the heat flowing into cavities is used to melt ice, and it is possible to define a thermal efficiency δ_{th} for each cavity

$$\delta_{th} = \frac{H_{LAT}}{H_{IN}}. \quad (5)$$

The numerator in (5) is what melt costs, while the denominator is what is provided. A "melting efficiency" was previously introduced by *Little et al*. [2009] and *Bindschadler et al*. [2011]. While our thermal efficiency is similar to the melting efficiency calculated by *Bindschadler et al*. [2011], it is slightly different from the one defined by *Little et al*. [2009], which was based on calculations of entrained water and heat. In this paper, we prefer to use the term "thermal efficiency" by contrast with the dynamical efficiency introduced above. The thermal efficiency δ_{th} is theoretically between 0 and 1, and the part of heat inflow that leaves a cavity can be expressed as $(1-\delta_{th})$. For Pine Island, we find a thermal efficiency of 19% in the reference experiment, in good agreement with the 22% calculated by *Bindschadler et al*. [2011] from a simulation, and with the 23 ± 6% recalculated from *Dutrieux et al*. [2014]'s observational data. In the other cavities, thermal efficiency is typically between 6 and 31% (Table 2). In other words, 69–94% of the heat that had melting potential leaves cavities without being used to melt ice shelves. This result is in qualitative agreement with *Jenkins* [1999] who reported a significant amount of CDW entrained by buoyant plumes in the Amundsen Sea.

The heat inflow and outflow in each cavity varies linearly with the total melt rate in each cavity (Figures 9b and 9c), mostly because heat transport is approximately proportional to volume transport (Figure 9a). The coefficient of proportionality (slope in Figure 9a) is mostly related to the overall thermal forcing in front of each cavity (see Appendix D), and the linearity is likely found because the thermal forcing in front of the cavities is essentially unchanged across the simulations. In Appendix D, we also show that a consequence of these linearities is that the thermal efficiency of each cavity (δ_{th}) increases with the total melt rate and tends to saturate for high melt rates. Thermal efficiency reaches a maximum value when the melt-induced transport overwhelms the background transport, i.e., when both H_{LAT} and H_{IN} are approximately proportional to the total melt rate. The maximum thermal efficiency ($\delta_{th\max}$) is inversely proportional to the dynamical efficiency (η_{dyn}) because the melt-induced heat inflow (i.e., induced by the dynamical pump) brings more energy than what is used for melt. For example, we have seen that 1 mSv of additional melt can lead to an additional 100–500 mSv into the cavity. In terms of energy, melting 1 mSv requires 0.34 TW while 100–500 mSv of water at 3.5°C above the freezing point corresponds to a supply of 1.4–7.1 TW. So for cavities with a very efficient dynamical pump (e.g., Thwaites, see slope in Figure 7c), the thermal efficiency is small (Figure 9d), and a lot of heat flows out of the cavity (Figure 9c). For cavities with a less efficient dynamical pump (e.g., Abbot), the melt-induced circulation brings relatively less heat when melt increases, so the thermal efficiency is higher, and less heat flows out of the cavity. In terms of characteristic timescales, a δ_{th} smaller than unity means that the characteristic residence time is shorter than the characteristic time of heat transfer to and over the entire ice/ocean interface.

To summarize, all the cavities have a melt-induced circulation, but the circulation sensitivity to melt depends on the characteristics of each cavity (e.g., its grounding line depth, size, ice draft slopes, and background density profile). When a strong circulation is induced by melt, any additional melt produces more inflow of heat into the cavity. In presence of CDW, the associated heat input is much larger than what is consumed by the additional melt, and the amount of heat exported from the cavity increases. When melt-induced circulation is weak or only represents a fraction of the total circulation, any additional melt does not produce much more heat inflow into the cavity, so a larger proportion of it is consumed by melting ice and a smaller amount of heat is exported from the cavity.

We now investigate the impact of changing ice-shelf melt rates on sea-ice volume. The later decreases for increasing ice-shelf melt (Figure 10). The largest sea-ice sensitivity to melt rate is found near the ice sheet/shelf front, and it is particularly strong near the area of Thwaites, Dotson, and Crosson where a 50% increase in melt rates (from present-day value) would typically decrease sea-ice volume by 4 ± 2% (Figure 10).

To further understand the sea-ice sensitivity to ice-shelf melt, we accumulate all the terms of the heat equation that contribute to set the annual mean temperature in the last simulation year

$$\underbrace{\partial_t T}_{\text{RATE}} = \underbrace{-u\partial_x T - v\partial_y T}_{\text{HADV}} \underbrace{-w\partial_z T}_{\text{VADV}} \underbrace{+D_l(T)}_{\text{HDIF}} \underbrace{+D_z(T)}_{\text{VDIF}} \underbrace{+I(T,z)}_{\text{SFLX}}, \quad (6)$$

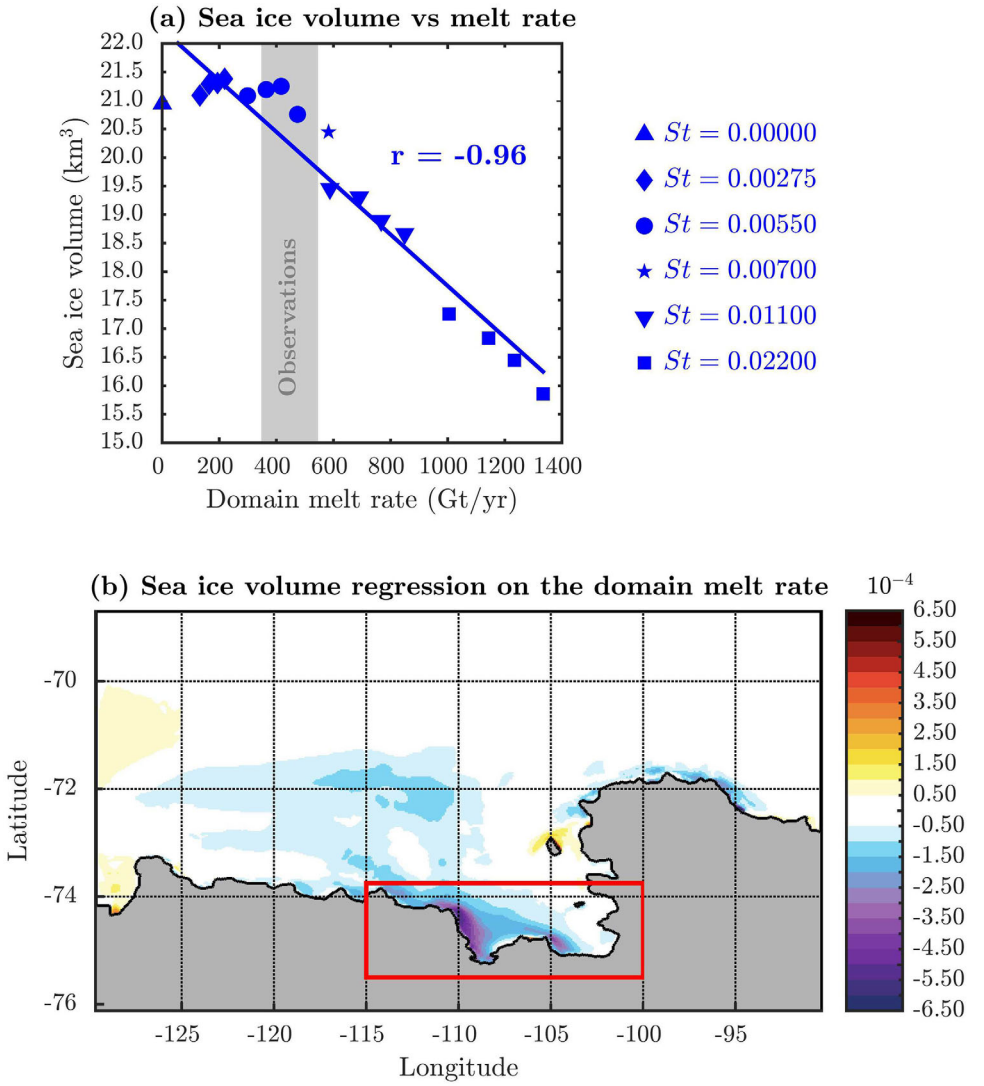

Figure 10. (a) Total sea-ice volume in the red box shown in the lower panel versus total melt rate underneath all the ice shelves represented in the model. Each marker represents a simulation with a particular value of (C_d,Γ_T), and means are calculated over the fifth year of simulation. The line indicates the least-mean-square regression, with corresponding correlation (r) indicated on the plot. The melt rate observational range is indicated in gray. (b) Regression coefficient of the local sea-ice volume on the total melt rate underneath all the ice shelves (units are m^3 of sea ice per m^2 per Gt yr^{-1}).

where HADV and VADV stand for horizontal and vertical heat advection, HDIF and VDIF for horizontal and vertical heat diffusion (mixing, including enhanced mixing related to parameterized convection), and SFLX for the contribution of surface heat fluxes at the air/sea and sea-ice/sea interfaces. Then, we use the decomposition of (6) to understand the difference in annual ocean temperatures between the various simulations and the simulation with no melt on the last simulation year

$$\overline{\Delta T}^{yr5} = \frac{1}{N_d} \sum_{d \in yr5} \int_{t=0}^{d} (\mathrm{HADV}(t) - \mathrm{HADV}_0(t) + \cdots + \mathrm{SFLX}(t) - \mathrm{SFLX}_0(t)) dt, \quad (7)$$

where N_d is the number of days in year 5, $t = 0$ corresponds to the initial state of the simulation, and subscripts 0 refer to the simulation with no melt ($\Gamma_T = 0$). All these quantities are then averaged horizontally within the box shown in Figure 10b that covers the area where sea ice is most sensitive to ice-shelf melt (not including cavities).

As shown in the previous section, more heat is exported from the cavities for stronger ice-shelf melt (Figure 9c), which is equivalent to more heat imported into the open ocean through horizontal heat advection

below ~75 m (Figure 11b). This does not significantly warm the ocean (Figure 11a) because most of this heat is then transported to upper levels through vertical advection (Figure 11c). This extra heat is partly removed by horizontal advection above ~75 m (Figure 11b), and the rest is removed from the near subsurface by vertical diffusion (Figure 11e). At the surface, stronger ice-shelf melt induces stronger cooling trend because sea-ice formation is associated with a latent heat uptake by surrounding waters, so less sea-ice formation (or more sea-ice melt) is associated with less heat uptake by the sea surface. However, changes in latent heat uptake at the surface only represents ~2% of the nonsolar fluxes, and the remaining anomaly is explained by a feedback leading to stronger heat loss through turbulent and longwave air-sea fluxes in simulations with less sea ice (not shown). This feedback is partly compensated by an opposite feedback whereby less sea ice leads to stronger penetration of solar fluxes into the ocean (Figure 11f). The negative peak related to vertical advection at 10 m (balanced by a positive peak related to vertical diffusion) would require further investigation, but it could be related to the summer turbocline (typically in the 10–20 m range) that is shallower for stronger ice-shelf melt (not shown); a shallower turbocline changes the depth where vertical

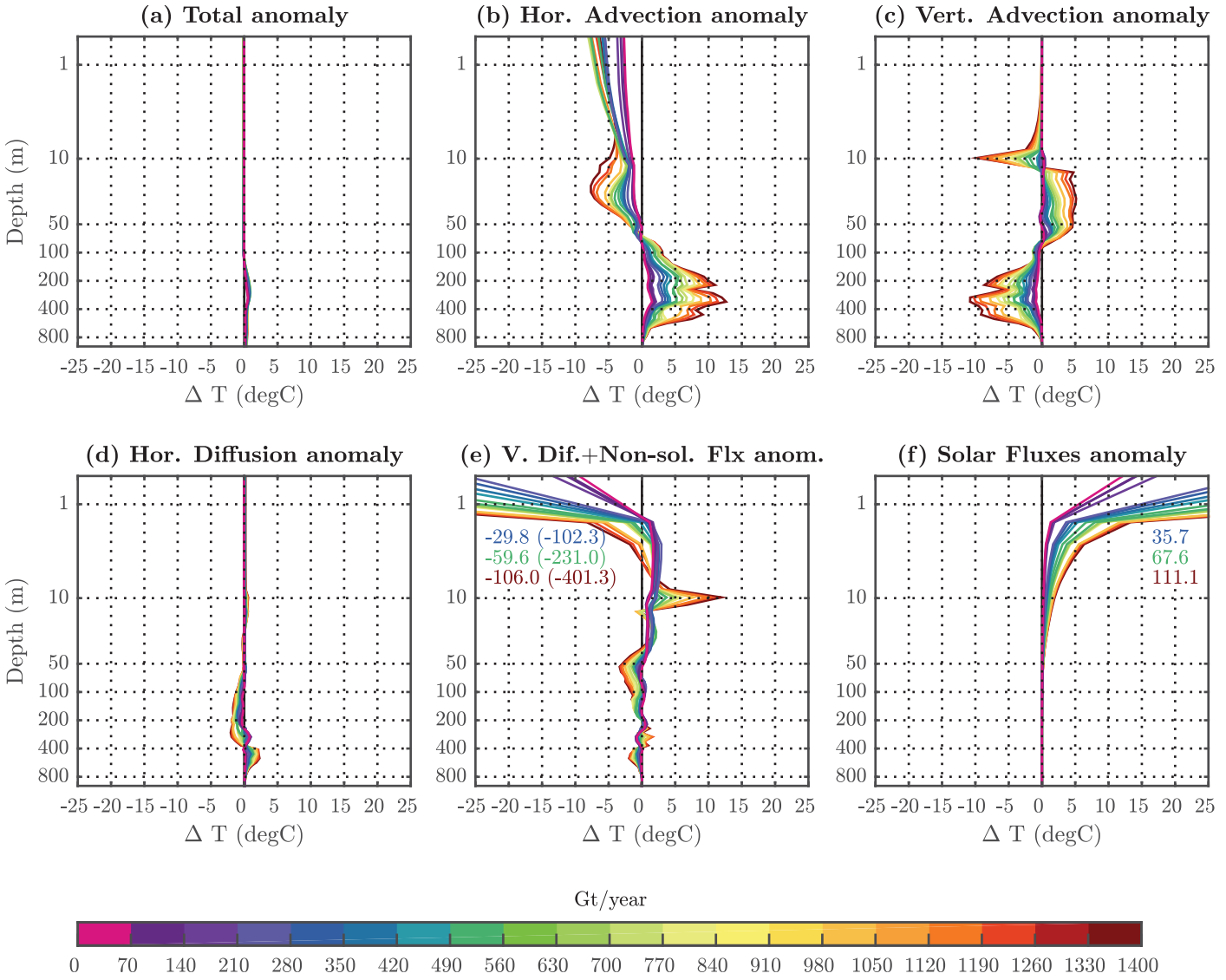

Figure 11. (a) Mean temperature profile anomaly with respect to the simulation with no melt ($\Gamma_T = 0$). The mean temperatures are calculated over the fifth year and within the red box shown in Figure 10b without including ice-shelf cavities. Each profile represents a simulation with a particular set of (C_d,Γ_T), and its color corresponds to the total melt rate in the domain. (b–f) Contributions of heat equation terms to the temperature anomaly shown in Figure 11a, calculated following (7). Figure 11e shows the sum of the contributions of vertical diffusion and nonsolar surface fluxes; these fluxes have a nonzero effect only at the upper model level (0.5 m), where the anomaly is negative and reaches as much as −400 K, ~3/4 of which is compensated by vertical diffusion. Some near-surface extreme values out of the *x* axis range in Figures 11e and 11f are indicated for three simulations; the numbers in brackets in Figure 11e are the nonsolar flux contributions alone.

advection (e.g., due to Ekman pumping) interacts with vertical mixing. Analyzing the terms of the sea-ice production budget as in *Rousset et al*. [2015] indicates that more ice-shelf melt water contributes to decrease sea-ice production through stronger bottom melt throughout the year (not shown). Such analysis also shows that complex feedbacks occur in winter, with rafting/ridging processes (and associated freezing of trapped seawater) contributing to weaker sea-ice production in presence of stronger ice-shelf melt, and a partial compensation by stronger bottom sea-ice growth in presence of stronger ice-shelf melt (not shown).

6. Conclusion

In this paper, we have made use of the newly developed ice-shelf capability in NEMO to simulate the ocean circulation in the Amundsen Sea region. We have first investigated melt sensitivity to the drag (C_d) and heat exchange (Γ_T) coefficients. At zero-order, melt is a function of the thermal Stanton number ($St_T = \sqrt{C_d}\Gamma_T$), and for a given St_T, melt is slightly higher for lower C_d values. In our case, these coefficients are uniform, but real cavities likely exhibit nonuniform and anisotropic surface roughness, e.g., due to the presence of channels or crevasses. In a similar way as sastrugi and associated roughness respond to wind variations at the ice sheet surface [e.g., *Amory et al*., 2016], roughness at the ice/ocean interface likely responds to melt variations and complex feedbacks may occur. At this stage, there are however not enough measurements of top boundary layer structures to estimate the importance of such nonuniformities.

These sensitivity tests have then been used to get further insights into the melt-induced ocean circulation. The volume transport into a cavity increases linearly with the ice-shelf melt rate and is associated with both an overturning and a barotropic circulation within the cavity. We have found that the melt-induced volume transport into a cavity is 100–500 times stronger than the melt volume flux itself, and we have called this factor of proportionality "efficiency of the dynamical pump." A simple model based on a potential energy budget has been proposed to better understand the factors controlling the dynamical efficiency. In short, the dynamical pump is very efficient for dense CDW and deep grounding lines, and poorly efficient if the water entering the deepest part of the cavity has a density close to the meltwater density. In front of the ice shelves, the barotropic transport by the coastal current also increases linearly with melt rates in cavities, so that a large part of the current transport is explained by ice-shelf melt. This emphasizes the importance to represent ice shelves in any ocean model aiming to represent the interactions between the deep ocean and the marginal seas or the interactions between adjacent seas (e.g., Amundsen Sea-Ross Sea).

Finally, we have investigated the heat transport sensitivity to melt rates. It is interesting to note that if the efficiency of the dynamical pump were weak, say 1 mSv of inflow induced by 1 mSv of melt, the CDW would need to be more than 70°C above the freezing point to sustain such melt rate. Thanks to the very efficient dynamical pump, the CDW inflow typically brings 4–20 times more heat than the latent heat required for melt. The extra heat is entrained by the buoyant plume and is exported toward the open ocean in front of the ice shelf. In our reference experiment, we have found that 6–31% of the heat that enters a cavity with melting potential is actually used to melt the ice shelf, which is consistent with observational estimates for Pine Island. This process is likely important for the consumption of CDW, and more generally for the heat budget of the upper 1000 m part of the ocean, and should be included in budgets of the global overturning circulation.

The heat that is transported out of the cavity is still buoyant and is therefore advected upward in front of the ice shelf. A part of this heat is carried away from the ice-shelf front by horizontal advection, but most of it reaches the ocean surface layer near the ice-shelf front where vertical mixing transfers the heat to sea ice. Therefore, we find that sea-ice volume along the ice sheet margins decreases significantly for higher melt rates in cavities. Hence, a part of the sea ice trend observed over the last decades in the Amundsen Sea [*Parkinson and Cavalieri*, 2012; *Turner et al*., 2009, 2013] could be explained by an increase in ice-shelf melt. These findings are strong incentives to include realistic ice-shelf meltwater fluxes in climate models, either using explicit cavities or using parameterizations [e.g., *Merino et al*., 2016b; *Pauling et al*., 2016; P. Mathiot et al., unpublished manuscript, 2017].

An interesting question remains as to whether our results, based on modified (C_d,Γ_T), can provide relevant information about simulated melt sensitivity to ocean warming. Looking at (1), it appears that doubling the thermal forcing is equivalent to homogeneously doubling the thermal Stanton number St_T. A difference is that C_d (and therefore St_T) affects the dynamics through friction, but we have shown that the circulation in a

cavity (at least in the Amundsen Sea) is much more controlled by the total melt rate in that cavity than by the exact C_d value (Figure 7). So our results on dynamical and thermal efficiency can probably be used to infer the effects of ocean warming, excluding complex but likely significant ocean/atmosphere and ice/ocean feedbacks. Finally, while temperatures have a direct effect on melt rates, densities control the melt-induced circulation (as shown in Appendix C), and future changes in salinity along the ice sheet margins are probably as important as changes in temperatures.

Appendix A

Here is summarized the background on drag and heat transfer coefficients. The turbulent heat flux Q (in W m^{-2}) between the top ocean mixed layer (TML) and the ice-shelf base is usually calculated as

$$Q=\rho_w c_{pw}\gamma_T(T_b-T_{TML}), \tag{A1}$$

where ρ_w and c_{pw} are the reference density and heat capacity of seawater, γ_T is the heat transfer velocity, and (T_b-T_{TML}) the thermal forcing, i.e., the difference between the conservative temperature at the ice-shelf base (i.e., conservative temperature at which seawater freezes) and the TML conservative temperature. Previous studies have sometimes considered γ_T as constant [e.g., *Hellmer and Olbers*, 1989; *Scheduikat and Olbers*, 1990; *Kusahara and Hasumi*, 2013], but most recent studies [e.g., *Dansereau et al.*, 2014] define γ_T as

$$\gamma_T=\Gamma_T u_\star, \tag{A2}$$

where $u_\star$ is the friction velocity and Γ_T is referred to as the turbulent heat transfer coefficient. The friction velocity $u_\star$ can be calculated as

$$u_\star=\sqrt{C_d u_{TML}^2}, \tag{A3}$$

where C_d is the drag coefficient accounting for surface roughness and affecting velocity shear (i.e., momentum transfer), and u_{TML} is the TML velocity.

The definition of γ_T has an impact on simulated melt rates. For instance, strongest melt rates along the buoyant meltwater plume are found in simulations with velocity-dependent γ_T but not in simulations with constant γ_T that are only thermally forced [*Dansereau et al.*, 2014]. Using constant γ_T also implies that any tuning to match observations is site-specific [*Jenkins et al.*, 2010]. Some studies use sophisticated formulations of Γ_T, derived from laboratory experiments, in which Γ_T is a function of $u_\star$, stability parameters, and constants from the similitude theory [*Jenkins*, 1991; *Holland and Jenkins*, 1999]. Nonetheless, the benefit of using such complex formulation rather than constant Γ_T is not clear [*Jenkins et al.*, 2010; *Walker et al.*, 2013], and we use constant Γ_T in this paper. Similar equations are used for salt exchange, with parameters referred to as γ_S and Γ_S.

Looking at (A1) and (A2), the thermal Stanton number [e.g., *McPhee et al.*, 1987] can be expressed as

$$St_T=\Gamma_T\sqrt{C_d}. \tag{A4}$$

This nondimensional number expresses the balance between heat transfer and the rate of change in heat capacity, i.e., $Q/(\rho_w c_{pw} u_{TML})$ [*Jenkins et al.*, 2010]. The thermal Stanton number is reminiscent of the bulk transfer coefficient for heat that is used to describe atmospheric surface layers [e.g., *Stull*, 2012]. A haline Stanton number St_S can be defined similarly from Γ_S.

To our knowledge, the only observational study that attempted to estimate the aforementioned coefficients from observations is by *Jenkins et al.* [2010] who combined measurements from a thermistor cable installed within the first 25 m beneath Ronne ice shelf [*Nicholls et al.*, 1997] and ice-penetrating radar. They found a thermal Stanton number in the 0.0011–0.0016 range at their single study site, but warned that the robustness of this estimate should be evaluated with an extended range of basal roughness characteristics, water temperatures, and tidal regimes. Moreover, their work did not allow separating C_d and Γ_T estimates (unless assuming that one of them is known). Other instrument lines have been deployed beneath ice-shelves [e.g., *Nicholls et al.*, 2012; *Stern et al.*, 2013; *Arzeno et al.*, 2014], but transfer coefficients have not been estimated or reported. In fact, most modeling studies so far have used a drag coefficient C_d with typical values in the 10^{-3} to 10^{-2} range [e.g., *Millgate et al.*, 2013; *De Rydt et al.*, 2014; *Dansereau et al.*, 2014], corresponding to those reported in sea-ice studies.

Table B1. Melts Rates in the Reference NEMO Simulation and Values Reported in the Literature for Ice-Shelf Cavities in the Amundsen Sea[a]

Ice-Shelf Name	Simulation or Reference	Mean Melt Rate (m w eq/yr)	Total Melt Flux (Gt/yr)	Method
Getz	AMU12.L75-REF	11.4 ± 0.7	290 ± 17	Mod. (∼3 km)
	Nakayama et al. [2014b]	3.8	127	Mod. (∼2.5 km)
	Nakayama et al. [2014a]	3.5	116	Mod. (∼2.5 km)
	Schodlok et al. [2016]	9.7 ± 0.8	261 ± 23	Mod. (∼18 km)
	St-Laurent et al. [2015]	7.0 ± 0.9		Mod. (1.5 km)
	Dinniman et al. [2015]	0.7 ± 0.3		Mod. (10 km)
	Timmermann et al. [2012]	5.4	164	Mod. (∼4 km)
	Kusahara and Hasumi [2013]	0.9 ± 0.1	32 ± 5	Mod. (10–20 km)
	Depoorter et al. [2013]	4.1 ± 0.7	136 ± 23	Input/output
	Rignot et al. [2013]	4.3 ± 0.4	145 ± 14	Input/output
	Jacobs et al. [2013]	2.6 ± 1.5		Ocean Obs.
Dotson	AMU12.L75-REF	6.8 ± 1.2	26 ± 5	Mod. (∼3 km)
	Nakayama et al. [2014a]	4.5	20	Mod. (∼2.5 km)
	Kusahara and Hasumi [2013]	0.7 ± 0.2	4 ± 1	Mod. (10–20 km)
	St-Laurent et al. [2015]	3.7 ± 0.5		Mod. (1.5 km)
	Rignot et al. [2013]	7.8 ± 0.6	45 ± 4	Input/output
Crosson	AMU12.L75-REF	2.9 ± 0.4	9 ± 1	Mod. (∼3 km)
	Nakayama et al. [2014a]	1.7	3	Mod. (∼2.5 km)
	Kusahara and Hasumi [2013]	0.4 ± 0.1	1 ± 1	Mod. (10–20 km)
	St-Laurent et al. [2015]	4.6 ± 0.2		Mod. (1.5 km)
	Rignot et al. [2013]	11.9 ± 1.0	38 ± 4	Input/output
Crosson + Dotson	AMU12.L75-REF	5.1 ± 1.6	35 ± 6	Mod. (∼3 km)
	Schodlok et al. [2016]	5.1 ± 0.6	50 ± 6	Mod. (∼18 km)
	Depoorter et al. [2013]	9.5 ± 0.8	78 ± 7	Input/output
Thwaites	AMU12.L75-REF	14.4 ± 1.2	58 ± 5	Mod. (∼3 km)
	Nakayama et al. [2014a]	7.7	27	Mod. (∼2.5 km)
	Schodlok et al. [2016]	7.2 ± 2.3	35 ± 11	Mod. (∼18 km)
	St-Laurent et al. [2015]	19.3 ± 1.8		Mod. (1.5 km)
	Kusahara and Hasumi [2013]	1.7 ± 0.2	9 ± 1	Mod. (10–20 km)
	Depoorter et al. [2013]	15.2 ± 3.9	69 ± 18	Input/output
	Rignot et al. [2013]	17.7 ± 1.0	97 ± 7	Input/output

[a]The area and period differ across the estimates. Basal melt rates are expressed in meters of pure water equivalent (m w eq) per year (i.e., t m^{-2} y^{-1}), and have been recalculated from meters of ice per year when necessary. The last column indicates the method used to estimate melt fluxes: ocean modeling (Mod., with model resolution into brackets), input/output method based on satellite observations and simulated surface mass balance, and oceanographic observations (Obs.). *Schodlok et al.* [2016]'s estimates are taken from their L100 experiment.

Appendix B

Here is given a complete assessment of simulated melt rates compared to observational and modeling estimates from the literature. Tables B1 and B2 gather observational values, either from input/output methods or from oceanographic measurements (through geostrophic calculations), and values from state-of-the-art ocean modeling studies. All these estimates cover different periods and have therefore to be considered as a broad estimate of what is expected in our simulations. Both the mean melt rate (in m yr^{-1}) and the total melt flux (in Gt yr^{-1}) are shown in Tables B1 and B2 because some observational studies have only reported one of these estimates, and because the ice-shelf area under consideration varies from one study to another. The comparison to input/output methods is detailed in section 3. Oceanographic estimates give weaker melt rates for Pine Island and Getz, which would make our model biases larger. Finally, our model biases are of comparable magnitude to the other recent modeling studies.

Appendix C

Here we propose an analytical expression for the dynamical efficiency introduced in section 4. For this purpose, we consider a cavity where the front has the same width L at all depths above seafloor, and we assume a simple overturning flow, consisting of a deep inflow that typically represents CDW, above which is an outflow representative of waters along the ice-shelf front that we hereafter refer to as winter waters (WWs) even though it can be waters in between CDW and WWs if the thermocline is shallower than the ice draft at the ice-shelf front. This simple overturning representation means that the barotropic flow is

Table B2. Continuation of Table B1[a]

Ice-Shelf Name	Simulation or Reference	Mean Melt Rate (m w eq/yr)	Total Melt Flux (Gt/yr)	Method
Pine Island	AMU12.L75-REF	22.2 ± 1.0	125 ± 6	Mod. (∼3 km)
	Nakayama et al. [2014b]	6.6	31	Mod. (∼2.5 km)
	Nakayama et al. [2014a]	7.2	34	Mod. (∼2.5 km)
	Schodlok et al. [2016]	12.3 ± 0.9	83 ± 6	Mod. (∼18 km)
	Dinniman et al. [2015]	1.6 ± 1.0		Mod. (10 km)
	St-Laurent et al. [2015]	13.9 ± 0.9		Mod. (1.5 km)
	Dansereau et al. [2014]	14.0 ± 5.0		Mod. (∼1 km)
	Dutrieux et al. [2014]		78 ± 18	Mod. (400 m)
	Kusahara and Hasumi [2013]	1.2 ± 0.2	9 ± 1	Mod. (10–20 km)
	Timmermann et al. [2012]	3.1	13	Mod. (∼4 km)
	Depoorter et al. [2013]	16.0 ± 2.4	95 ± 14	Input/output
	Rignot et al. [2013]	16.2 ± 1.0	101 ± 8	Input/output
	Jacobs et al. [2011]		63 ± 15	Ocean Obs.
	Dutrieux et al. [2014]		68 ± 34	Ocean Obs.
Cosgrove	AMU12.L75-REF	6.8 ± 1.4	20 ± 4	Mod. (∼3 km)
	Schodlok et al. [2016]	7.6 ± 1.3	30 ± 5	Mod. (∼18 km)
	St-Laurent et al. [2015]	6.4 ± 0.5		Mod. (1.5 km)
	Nakayama et al. [2014a]	5.7	12	Mod. (∼2.5 km)
	Kusahara and Hasumi [2013]	0.6 ± 0.1	3 ± 1	Mod. (10–20 km)
	Depoorter et al. [2013]	3.8 ± 0.9	11 ± 3	Input/output
	Rignot et al. [2013]	2.8 ± 0.7	8 ± 2	Input/output
Abbot	AMU12.L75-REF	3.0 ± 0.4	85 ± 13	Mod. (∼3 km)
	Schodlok et al. [2016]	1.0 ± 0.3	32 ± 10	Mod. (∼18 km)
	Dinniman et al. [2015]	0.3 ± 0.2		Mod. (10 km)
	St-Laurent et al. [2015]	1.7 ± 0.1		Mod. (1.5 km)
	Nakayama et al. [2014b]	1.8	55	Mod. (∼2.5 km)
	Nakayama et al. [2014a]	1.7	50	Mod. (∼2.5 km)
	Kusahara and Hasumi [2013]	1.4 ± 0.4	45 ± 15	Mod. (10–20 km)
	Timmermann et al. [2012]	2.1	59	Mod. (∼4 km)
	Depoorter et al. [2013]	2.7 ± 0.7	86 ± 22	Input/output
	Rignot et al. [2013]	1.9 ± 0.6	52 ± 19	Input/output

[a]*Dansereau et al.* [2014]'s estimates for Pine Island are taken from their experiments with velocity-dependent transfer coefficients.

neglected, and we assume that the ocean density and velocity across the front of the cavity as well as melt rates in the cavity are respectively given by

$$\begin{cases} \rho(z) = \rho_{WW} & \text{for } z < z_{1/2} \\ \quad\;\; = \rho_{CDW} & \text{for } z \geq z_{1/2} \\ u(z) = -\Phi_{OUT}/L(z_{1/2} - z_t) & \text{for } z < z_{1/2} \\ \quad\;\; = \Phi_{IN}/L(z_b - z_{1/2}) & \text{for } z \geq z_{1/2} \\ m(z) = 0 & \text{for } z < z_{1/2} \\ \quad\;\; = m_0 & \text{for } z \geq z_{1/2} \end{cases}, \tag{C1}$$

where z is depth (positive), and z_b and z_t are, respectively, the bottom and top depth of the entrance of the cavity. Φ_{OUT} and Φ_{IN} are the volume transports entering and leaving the cavity, respectively (both defined positive). The depth of the interface between the two layers is $z_{1/2}$, it ensures volume conservation, i.e., $\Phi_{OUT} = \Phi_{IN} + M/\rho_m$, where ρ_m is the meltwater density and M the total melt rate (in mass per time units). $z_{1/2}$ is the median depth of the ice-shelf front if $M/\rho_m \ll \Phi_{IN}$.

In steady state, the potential energy of the water in the cavity (E_p) has to remain constant. Neglecting the power dissipated by friction along the seafloor and ice draft, and assuming that the input flow does not contribute to change E_p (because the density at depth is the same in front and inside the cavity), the source of potential energy is melt, and the sink is the outflow

$$\frac{dE_p}{dt} = \left(\frac{dE_p}{dt}\right)_M + \left(\frac{dE_p}{dt}\right)_{OUT} = 0. \tag{C2}$$

Given our approximations, we obtain

$$\left(\frac{dE_p}{dt}\right)_M = Mg\,\frac{\rho_{CDW}-\rho_m}{\rho_m}\,Z_{CDW}, \tag{C3}$$

where M is the total melt rate in kg s^{-1} and Z_{CDW} the mean depth of the ice draft in the CDW layer (weighted by the ice draft surface at each depth), and is $(z_{1/2}+z_b)/2$ if the cavity has the same width at all depths.

Accounting for dilution and cooling of the inflow under the ice shelf, it is possible to calculate the outflow density

$$\rho_{OUT} = \frac{\Phi_{IN}\rho_{CDW} + \left(1+\frac{\alpha L_f}{c_p}\right)M}{\Phi_{IN}+M/\rho_m} \simeq \frac{\Phi_{IN}\rho_{CDW}+M}{\Phi_{IN}+M/\rho_m}, \tag{C4}$$

where α is the thermal expansion coefficient. Using $\alpha = 3.87\times10^{-5}$ K^{-1} [*Jenkins*, 1991], we find that $\frac{\alpha L_f}{c_p} \ll 1$, which means that the buoyancy is mostly controlled by dilution. This yields

$$\left(\frac{dE_p}{dt}\right)_{OUT} = \Phi_{OUT}(\rho_{OUT}-\rho_{WW})\,gZ_{WW} = [\Phi_{IN}(\rho_{CDW}-\rho_{WW}) + \frac{M}{\rho_m}\,(\rho_m-\rho_{WW})]gZ_{WW}, \tag{C5}$$

where Z_{WW} is the mean depth of the WW layer, i.e., $(z_{1/2}+z_t)/2$ if we assume the same width L of the cavity front at all depths above seafloor.

Combining the three previous equations yields

$$\Phi_{IN} = \frac{(\rho_{CDW}-\rho_m)Z_{CDW}-(\rho_{WW}-\rho_m)Z_{WW}}{(\rho_{CDW}-\rho_{WW})Z_{WW}}\,\frac{M}{\rho_m} = \eta_{dyn}\,\frac{M}{\rho_m}, \tag{C6}$$

which can be further simplified for three asymptotic cases.

1. For dense CDW and relatively deep cavities, or for fresh WW, we have $(\rho_{CDW}-\rho_m)Z_{CDW} \gg (\rho_{WW}-\rho_m)Z_{WW}$, which yields

$$\eta_{dyn} \simeq \frac{\rho_{CDW}-\rho_m}{\rho_{CDW}-\rho_{WW}}\,\frac{Z_{CDW}}{Z_{WW}}. \tag{C7}$$

In this case, the dynamical pump will be highly efficient ($\eta_{dyn} \gg 1$) for deepest cavities and relatively dense WW.

2. For relatively light CDW (i.e., mixed with a lot of meltwater), i.e., $\rho_{CDW} \simeq \rho_m$, (C6) gives $\eta_{dyn} \simeq 1$. The same result is found for ice-shelves presenting a shallow water column, i.e., where $Z_{CDW} \simeq Z_{WW}$.
3. If the ocean is homogeneous in front of the ice shelf, i.e., if $\rho_{CDW} \simeq \rho_{WW}$, (C6) gives $\eta_{dyn} \simeq (Z_{CDW}-Z_{WW})/Z_{WW}$.

For large cavities, the power dissipated by friction might not be negligible. From an energy point of view, friction tends to decrease the efficiency of the dynamical pump because a part of the potential energy is dissipated instead of being used for the dynamical pump. From a dynamical point of view, friction induces upslope flow within a buoyant Ekman layer [*Jenkins*, 2016], which is expected to increase the overturning part of the transport compared to the barotropic part. In this paper, we find that for a given thermal Stanton number, different drag coefficients do not create very different circulations, so friction does not appear to play an important role in the circulation within the small cavities of the Amundsen Sea, but a stronger effect could be found for larger cavities.

The development proposed in this appendix is very simple and helps gain insights into the nature of the dynamical pump. Such energetical considerations could be used to improve the formulation of melt-induced inflows in simple ice-shelf box models [*Olbers and Hellmer*, 2010]. It is nonetheless important to keep in mind that this model does not include all the important aspects of a real cavity. For example, *Jenkins* [2016], from dynamical considerations, has suggested that the curvature of the ice-shelf base may play a role in driving the dynamical pump.

Appendix D

Here we provide some details on the heat budget calculation, and we indicate some consequences of the linear relationships found in sections 4 and 5.

Neglecting heat diffusion in ice and turbulent diffusion in the ocean interior, the heat budget of the ocean within an ice-shelf cavity can be written as

$$\begin{cases} & \rho_w c_p \iint_{r\in\text{front},u>0} u(r,z)\left(T(r,z)-T_f^0\right) dr\, dz & \ldots \mathrm{H_{IN}} \\ + & \rho_w c_p \iint_{r\in\text{front},u<0} u(r,z)\left(T(r,z)-T_f^0\right) dr\, dz & \ldots \mathrm{H_{OUT}} \\ + & \rho_w c_p \iint_{x,y\in\text{draft}} m\left(T_f(S,z)-T_f^0\right) dx\, dy & \ldots \mathrm{H_{MELT\ FLOW}}, \\ = & L_f \iint_{x,y\in\text{draft}} \rho_i m\, dx\, dy & \ldots \mathrm{H_{LAT}} \\ + & \rho_w c_p \iiint_{x,y,z\in\text{cavity}} \frac{dT(x,y,z)}{dt} dx\, dy\, dz & \ldots \mathrm{H_{HC\ VAR}} \end{cases} \tag{D1}$$

where $u(r, z)$ is the ocean velocity perpendicular to the ice-shelf front (positive into the cavity), $T(r, z)$ the conservative temperature along the front, $T_f(S, z)$ the conservative temperature of melted water at depth z, T_f^0 the freezing temperature at sea surface for a salinity of 34 g kg^{-1}, and other quantities were defined in section 2. Heat fluxes in equation (D1) are calculated with respect to the surface freezing temperature and can therefore be considered as a flux of heat with melting potential in the sense that any heat entering the cavity will potentially be transported by the buoyant and rotating flow along the ice draft and melt some ice at upper levels. A better estimate of this potential would be to consider the depth of the ice-shelf front, but for a sake of simplicity, we chose to use the surface as reference depth as in previous studies [*Ha et al.*, 2014]. The heat flux into the cavity ($\mathrm{H_{IN}}$) is partly used to melt ice ($\mathrm{H_{LAT}}$). Ice melt is associated with a volume flux at the freezing temperature at ice draft depth ($\mathrm{H_{MELT\ FLOW}}$), and some of the remaining heat flows out of the cavity ($\mathrm{H_{OUT}}$) or is used to cool or warm the water within the ice-shelf cavity ($\mathrm{H_{HC\ VAR}}$). $\mathrm{H_{MELT\ FLOW}}$ is typically 3–4 orders of magnitude smaller than $\mathrm{H_{IN}}$ in our simulations, and is therefore neglected in the following. In this paper, all the terms are calculated as yearly means from daily means of u, T, S, m. Over a year in steady state, $\mathrm{H_{HC\ VAR}}$ is close to zero, so this term is also neglected in the annual budgets, and (D1) can be simplified as

$$\mathrm{H_{IN}} + \mathrm{H_{OUT}} = \mathrm{H_{LAT}}. \tag{D2}$$

From Figure 7c and the definition of the dynamical efficiency (η_{dyn}) given in Appendix C and in section 4, the volume transport into the cavity can be written as

$$\Phi_{\mathrm{IN}} = \Phi_0 + \eta_{dyn} \frac{M}{\rho_w}, \tag{D3}$$

where M is the total melt rate (in kg s^{-1}) and Φ_0 is the background transport.

For most cavities, the heat transport into the cavity is directly proportional to the volume transport (Figure 9a)

$$\mathrm{H_{IN}} = \rho_w c_p \langle \mathrm{TF} \rangle \Phi_{\mathrm{IN}}, \tag{D4}$$

where $\langle \mathrm{TF} \rangle$ can be understood as an overall thermal forcing for a given cavity. Indeed, $\langle \mathrm{TF} \rangle$ is moderately correlated to the annual mean thermal forcing along the ice-shelf front between the grounding line depth and the median depth of the ice draft ($r = 0.67$, $p = 0.10$). Based on in situ observations, *Jenkins* [1999] found coefficients of proportionality of similar order of magnitude as our results (see

his Figure 12). Highest $\langle \mathrm{TF} \rangle$ are found for Pine Island, and lowest $\langle \mathrm{TF} \rangle$ are found for Crosson and Abbot (Figure 9a).

From (D2) and (D4), we deduce the input and output heat transport as well as the thermal efficiency

$$\begin{cases} \mathrm{H_{IN}} &= \rho_w c_p \langle \mathrm{TF} \rangle \Phi_0 + c_p \langle \mathrm{TF} \rangle \eta_{dyn} M \\ \mathrm{H_{OUT}} &= -\rho_w c_p \langle \mathrm{TF} \rangle \Phi_0 - (c_p \langle \mathrm{TF} \rangle \eta_{dyn} - L_f) M \\ \delta_{th} &= \dfrac{L_f M}{\rho_w c_p \langle \mathrm{TF} \rangle \Phi_0 + c_p \langle \mathrm{TF} \rangle \eta_{dyn} M} \end{cases}. \tag{D5}$$

These expressions match our simulations pretty well (dashed lines in Figures 9b–9d), apart for Dotson, and to a lower extent Crosson (not shown).

The thermal efficiency increases with total melt rate M and tends to saturate at a value of $\delta_{th\max}$ for large enough total melt rates, i.e., when melt-induced transport overwhelms the background transport, with

$$\delta_{th\max} = \frac{L_f}{\eta_{dyn} \langle \mathrm{TF} \rangle}. \tag{D6}$$

This shows that an efficient pump (large η_{dyn}) tends to be associated with a small thermal efficiency, i.e., a large part of the heat inflow induced by melt will flow out of the cavity without being used to melt the ice shelf. Similarly, high thermal forcing $\langle \mathrm{TF} \rangle$ is associated with a small thermal efficiency. Therefore, cavities with a weak thermal forcing and poorly efficient pump will be associated with a thermal efficiency close to 1. In this case, the heat inflow induced by melt is of similar magnitude as the melt latent heat flux, i.e., the heat inflow induced by melt is itself used to melt ice. By contrast, cavities with a strong thermal forcing and a very efficient pump will be associated with a low thermal efficiency, i.e., the melt-induced heat inflow is much larger than the melt latent heat flux, i.e., the melt-induced heat inflow brings so much heat that it cannot be entirely used for ice melting along its path in the cavity. This means that cavities with a weak overall thermal forcing and poorly efficient pump do not have any heat flowing out of the cavity with melting potential (i.e., above the freezing point), whereas cavities with a strong overall thermal forcing and a very efficient pump do have a lot of heat flowing out of the cavity with melting potential.

Acknowledgments
This work was funded by the French National Research Agency (ANR) through the TROIS-AS (ANR-15-CE01-0005-01) and SUMER (ANR-12-BS06-0018) projects. N.J., N.M., G.D., and J.L. are part of Labex OSUG@2020 (ANR10 LABX56). N.J. is an Associate Investigator of the ARC Centre of Excellence for Climate System Science. P.S. was supported by an Australian Research Council (ARC) DECRA Fellowship (DE150100223). The computational resources were provided by CINES through the egi6035 and gge6066 projects. We thank C. Rousset, M. Vancoppenolle. and J.-M. Molines for useful guidance in the development of the AMU12 configuration, and the ISOMIP+ and FRISP groups for useful discussions. The model code for NEMO-3.6 is available from the NEMO website (www.nemo-ocean.eu). The branch used in this study is the development branch named dev_r5151_UKMO_ISF at revision 5932.

References

Amory, C., F. Naaim-Bouvet, H. Gallée, and E. Vignon (2016), Brief communication: Two well-marked cases of aerodynamic adjustment of sastrugi, *Cryosphere*, *10*(2), 743–750.

Arzeno, I. B., R. C. Beardsley, R. Limeburner, B. Owens, L. Padman, S. R. Springer, C. L. Stewart, and M. J. M. Williams (2014), Ocean variability contributing to basal melt rate near the ice front of Ross Ice Shelf, Antarctica, *J. Geophys. Res. Oceans*, *119*, 4214–4233, doi:10.1002/2014JC009792.

Asay-Davis, X. S., et al. (2015), Experimental design for three interrelated Marine Ice-Sheet and Ocean Model Intercomparison Projects, *Geosci. Model Dev. Discuss.*, *8*(11), 9859–9924.

Assmann, K. M., A. Jenkins, D. R. Shoosmith, D. P. Walker, S. S. Jacobs, and K. W. Nicholls (2013), Variability of Circumpolar Deep Water transport onto the Amundsen Sea continental shelf through a shelf break trough, *J. Geophys. Res. Oceans*, *118*, 6603–6620, doi:10.1002/2013JC008871.

Bamber, J. L., R. E. M. Riva, B. L. A. Vermeersen, and A. M. LeBrocq (2009), Reassessment of the potential sea-level rise from a collapse of the West Antarctic Ice Sheet, *Science*, *324*(5929), 901–903.

Barnier, B., et al. (2006), Impact of partial steps and momentum advection schemes in a global ocean circulation model at eddy-permitting resolution, *Ocean Dyn.*, *56*(5–6), 543–567.

Bindschadler, R., D. G. Vaughan, and P. Vornberger (2011), Variability of basal melt beneath the Pine Island Glacier ice shelf, West Antarctica, *J. Glaciol.*, *57*(204), 581–595.

Church, J. A., et al. (2013), Sea-level rise by 2100, *Science*, *342*(6165), 1445–1445.

Dansereau, V., P. Heimbach, and M. Losch (2014), Simulation of subice shelf melt rates in a general circulation model: Velocity-dependent transfer and the role of friction, *J. Geophys. Res. Oceans*, *119*, 1765–1790, doi:10.1002/2013JC008846.

De Rydt, J., and G. H. Gudmundsson (2016), Coupled ice shelf-ocean modeling and complex grounding line retreat from a seabed ridge, *J. Geophys. Res. Earth Surf.*, *121*, 865–880, doi:10.1002/2015JF003791.

De Rydt, J., P. R. Holland, P. Dutrieux, and A. Jenkins (2014), Geometric and oceanographic controls on melting beneath Pine Island Glacier, *J. Geophys. Res. Oceans*, *119*, 2420–2438, doi:10.1002/2013JC009513.

Depoorter, M. A., J. L. Bamber, J. A. Griggs, J. T. M. Lenaerts, S. R. M. Ligtenberg, M. R. van den Broeke, and G. Moholdt (2013), Calving fluxes and basal melt rates of Antarctic ice shelves, *Nature*, *502*(7469), 89–92.

Dinniman, M. S., J. M. Klinck, and W. O. Smith (2011), A model study of Circumpolar Deep Water on the West Antarctic Peninsula and Ross Sea continental shelves, *Deep Sea Res., Part II*, *58*(13), 1508–1523.

Dinniman, M. S., J. M. Klinck, L.-S. Bai, D. H. Bromwich, K. M. Hines, and D. M. Holland (2015), The effect of atmospheric forcing resolution on delivery of ocean heat to the Antarctic floating ice shelves, *J. Clim.*, *28*(15), 6067–6085.

Downes, S. M., et al. (2015). An assessment of Southern Ocean water masses and sea ice during 1988–2007 in a suite of interannual CORE-II simulations, *Ocean Modell.*, *94*, 67–94.
Dutrieux, P., J. De Rydt, A. Jenkins, P. R. Holland, H. K. Ha, S. H. Lee, E. J. Steig, Q. Ding, E. P. Abrahamsen, and M. Schröder (2014), Strong sensitivity of Pine Island ice-shelf melting to climatic variability, *Science*, *343*(6167), 174–178.
Favier, L., G. Durand, S. L. Cornford, G. H. Gudmundsson, O. Gagliardini, F. Gillet-Chaulet, T. Zwinger, A. J. Payne, and A. M. Le Brocq (2014), Retreat of Pine Island Glacier controlled by marine ice-sheet instability, *Nat. Clim. Change*, *4*(2), 117–121.
Fretwell, P., et al. (2013), Bedmap2: Improved ice bed, surface and thickness datasets for Antarctica, *Cryosphere*, *7*, 375–393.
Griffies, S. M., et al. (2009), Coordinated ocean-ice reference experiments (COREs), *Ocean Modell.*, *26*(1), 1–46.
Gwyther, D. E., B. K. Galton-Fenzi, M. S. Dinniman, J. L. Roberts, and J. R. Hunter (2015), The effect of basal friction on melting and freezing in ice shelf–ocean models, *Ocean Modell.*, *95*, 38–52.
Ha, H. K., A. K. Wåhlin, T. W. Kim, S. H. Lee, J. H. Lee, H. J. Lee, C. S. Hong, L. Arneborg, G. Björk, and O. Kalén (2014), Circulation and modification of warm deep water on the central Amundsen Shelf, *J. Phys. Oceanogr.*, *44*(5), 1493–1501.
Hallberg, R. (2013), Using a resolution function to regulate parameterizations of oceanic mesoscale eddy effects, *Ocean Modell.*, *72*, 92–103.
Hellmer, H. H., and D. J. Olbers (1989), A two-dimensional model for the thermohaline circulation under an ice shelf, *Antarct. Sci.*, *1*(04), 325–336.
Heywood, K. J., R. A. Locarnini, R. D. Frew, P. F. Dennis, and B. A. King (1998), Transport and water masses of the Antarctic Slope Front system in the eastern Weddell Sea, *Antarct. Res. Ser.*, *75*, 203–214.
Holland, D. M., and A. Jenkins (1999), Modeling thermodynamic ice-ocean interactions at the base of an ice shelf, *J. Phys. Oceanogr.*, *29*(8), 1787–1800.
Hughes, T. (1973). Is the West Antarctic ice sheet disintegrating?, *J. Geophys. Res.*, *78*(33), 7884–7910.
IOC, SCOR, IAPSO (2010), The international thermodynamic equation of seawater - 2010: Calculation and use of thermodynamic properties, in *Intergovernmental Oceanographic Commission, Manuals and Guides No. 56, UNESCO (English)*, 196 pp.
Jacobs, S., A. Jenkins, H. Hellmer, C. Giulivi, F. Nitsche, B. Huber, and R. Guerrero (2012), The Amundsen Sea and the Antarctic ice sheet, *Oceanography*, *25*(3), 154–163.
Jacobs, S., C. Giulivi, P. Dutrieux, E. Rignot, F. Nitsche, and J. Mouginot (2013), Getz Ice Shelf melting response to changes in ocean forcing, *J. Geophys. Res. Oceans*, *118*, 4152–4168, doi:10.1002/jgrc.20298.
Jacobs, S. S., A. Jenkins, C. F. Giulivi, and P. Dutrieux (2011), Stronger ocean circulation and increased melting under Pine Island Glacier ice shelf, *Nat. Geosci.*, *4*(8), 519–523.
Jenkins, A. (1991), A one-dimensional model of ice shelf-ocean interaction, *J. Geophys. Res.*, *96*(C11), 20,671–20,677.
Jenkins, A. (1999), The impact of melting ice on ocean waters, *J. Phys. Oceanogr.*, *29*(9), 2370–2381.
Jenkins, A. (2016). A simple model of the ice shelf–ocean boundary layer and current, *J. Phys. Oceanogr.*, *46*(6), 1785–1803.
Jenkins, A., K. W. Nicholls, and H. F. J. Corr (2010), Observation and parameterization of ablation at the base of Ronne Ice Shelf, Antarctica, *J. Phys. Oceanogr.*, *40*, 2298–2312.
Joughin, I., B. E. Smith, and B. Medley (2014), Marine ice sheet collapse potentially under way for the Thwaites Glacier Basin, West Antarctica, *Science*, *344*(6185), 735–738.
Kusahara, K., and H. Hasumi (2013), Modeling Antarctic ice shelf responses to future climate changes and impacts on the ocean, *J. Geophys. Res.*, *118*, 2454–2475, doi:10.1002/jgrc.20166.
Large, W. G., and S. G. Yeager (2004), Diurnal to decadal global forcing for ocean and sea-ice models: The data sets and flux climatologies, *Tech. Rep. NCAR/TN-460+STR*, Natl. Cent. for Atmos. Res., Boulder, Colo.
Large, W. G., and S. G. Yeager (2009), The global climatology of an interannually varying air–sea flux data set, *Clim. Dyn.*, *33*(2–3), 341–364.
Lengaigne, M., G. Madec, L. Bopp, C. Menkes, O. Aumont, and P. Cadule (2009), Bio-physical feedbacks in the Arctic Ocean using an Earth system model, *Geophys. Res. Lett.*, *36*, L21602, doi:10.1029/2009GL040145.
Levitus, S., et al. (2012), World ocean heat content and thermosteric sea level change (0–2000 m), 1955–2010, *Geophys. Res. Lett.*, *39*, L10603, doi:10.1029/2012GL051106.
Lévy, M., A. Estublier, and G. Madec (2001), Choice of an advection scheme for biogeochemical models, *Geophys. Res. Lett.*, *28*(19), 3725–3728.
Lewis, E. L., and R. G. Perkin (1986), Ice pumps and their rates, *J. Geophys. Res.*, *91*(C10), 756–711.
Little, C. M., A. Gnanadesikan, and M. Oppenheimer (2009), How ice shelf morphology controls basal melting, *J. Geophys. Res.*, *114*, C12007, doi:10.1029/2008JC005197.
Losch, M. (2008), Modeling ice shelf cavities in az coordinate ocean general circulation model, *J. Geophys. Res.*, *113*, C08043, doi:10.1029/2007JC004368.
Madec, G., and NEMO-team (2016), NEMO ocean engine, version 3.6 stable, in Note du Pôle de modélisation de l'Institut Pierre-Simon Laplace No 27, IPSL, Paris, France.
Mankoff, K. D., S. S. Jacobs, S. M. Tulaczyk, and S. E. Stammerjohn (2012), The role of Pine Island Glacier ice shelf basal channels in deep-water upwelling, polynyas and ocean circulation in Pine Island Bay, Antarctica, *Ann. Glaciol.*, *53*(60), 123–128.
McPhee, M. (2008), *Air-Ice-Ocean Interaction: Turbulent Ocean Boundary Layer Exchange Processes*, Springer, New York.
McPhee, M. G., G. A. Maykut, and J. H. Morison (1987), Dynamics and thermodynamics of the ice/upper ocean system in the marginal ice zone of the Greenland Sea, *J. Geophys. Res.*, *92*(C7), 7017–7031.
Meier, W., F. Fetterer, M. Savoie, S. Mallory, R. Duerr, and J. Stroeve (2013), NOAA/NSIDC climate data record of passive microwave sea ice concentration, Version 2, Natl. Snow and Ice Data Cent., Boulder, Colo., doi:http://dx.doi.org/10.7265/N55M63M1.
Mercer, J. H. (1968), Antarctic ice and Sangamon sea level, *Contrib. No. 139*, technical report, Inst. of Polar Stud., Ohio State Univ., Columbus.
Mercer, J. H. (1978), West Antarctic ice sheet and CO_2 greenhouse effect—A threat of disaster, *Nature*, *271*(5643), 321–325.
Merino, N., J. Le Sommer, G. Durand, N. C. Jourdain, G. Madec, P. Mathiot, and J. Tournadre (2016b), Antarctic icebergs melt over the Southern Ocean: Climatology and impact on sea-ice, *Ocean Modell.*, *104*, 99–110.
Millgate, T., P. R. Holland, A. Jenkins, and H. L. Johnson (2013), The effect of basal channels on oceanic ice-shelf melting, *J. Geophys. Res. Oceans*, *118*, 6951–6964, doi:10.1002/2013JC009402.
Mouginot, J., E. Rignot, and B. Scheuchl (2014), Sustained increase in ice discharge from the Amundsen Sea Embayment, West Antarctica, from 1973 to 2013, *Geophys. Res. Lett.*, *41*, 1576–1584, doi:10.1002/2013GL059069.
Nakayama, Y., R. Timmermann, C. B. Rodehacke, M. Schröder, and H. H. Hellmer (2014a), Modeling the spreading of glacial meltwater from the Amundsen and Bellingshausen Seas, *Geophys. Res. Lett.*, *41*, 7942–7949, doi:10.1002/2014GL061600.
Nakayama, Y., R. Timmermann, M. Schröder, and H. H. Hellmer (2014b), On the difficulty of modeling Circumpolar Deep Water intrusions onto the Amundsen Sea continental shelf, *Ocean Modell.*, *84*, 26–34.

Nicholls, K. W., K. Makinson, and M. R. Johnson (1997), New oceanographic data from beneath Ronne ice shelf, Antarctica, *Geophys. Res. Lett.*, *24*(2), 167–170.
Nicholls, K. W., K. Makinson, and E. J. Venables (2012), Ocean circulation beneath Larsen C Ice Shelf, Antarctica from in situ observations, *Geophys. Res. Lett.*, *39*, L19608, doi:10.1029/2012GL053187.
Olbers, D., and H. Hellmer (2010), A box model of circulation and melting in ice shelf caverns, *Ocean Dyn.*, *60*(1), 141–153.
O'Reilly, J. E., S. Maritorena, B. G. Mitchell, D. A. Siegel, K. L. Carder, S. A. Garver, M. Kahru, and C. McClain (1998), Ocean color chlorophyll algorithms for SeaWiFS, *J. Geophys. Res.*, *103*(C11), 24,937–24,953.
Özgökmen, T. M., E. P. Chassignet, and C. G. H. Rooth (2001), On the connection between the Mediterranean outflow and the Azores Current, *J. Phys. Oceanogr.*, *31*(2), 461–480.
Parkinson, C. L., and D. J. Cavalieri (2012), Antarctic sea ice variability and trends, 1979–2010, *Cryosphere*, *6*(4), 871–880.
Pauling, A. G., C. M. Bitz, I. J. Smith, and P. J. Langhorne (2016), The response of the Southern Ocean and Antarctic Sea Ice to freshwater from ice shelves in an earth system model, *J. Clim.*, *29*, 1655–1672.
Payne, A. J., A. Vieli, A. P. Shepherd, D. J. Wingham, and E. Rignot (2004), Recent dramatic thinning of largest West Antarctic ice stream triggered by oceans, *Geophys. Res. Lett.*, *31*, L23401, doi:10.1029/2004GL021284.
Payne, A. J., P. R. Holland, A. P. Shepherd, I. C. Rutt, A. Jenkins, and I. Joughin (2007), Numerical modeling of ocean-ice interactions under Pine Island Bays ice shelf, *J. Geophys. Res.*, *112*, C10019, doi:10.1029/2006JC003733.
Petty, A. A., P. R. Holland, and D. L. Feltham (2014), Sea ice and the ocean mixed layer over the Antarctic shelf seas, *Cryosphere*, *8*(2), 761–783.
Rignot, E., S. Jacobs, J. Mouginot, and B. Scheuchl (2013), Ice-shelf melting around Antarctica, *Science*, *341*(6143), 266–270.
Rignot, E., J. Mouginot, M. Morlighem, H. Seroussi, and B. Scheuchl (2014), Widespread, rapid grounding line retreat of Pine Island, Thwaites, Smith, and Kohler glaciers, West Antarctica, from 1992 to 2011, *Geophys. Res. Lett.*, *41*, 3502–3509, doi:10.1002/2014GL060140.
Robertson, R. (2013), Tidally induced increases in melting of Amundsen Sea ice shelves, *J. Geophys. Res. Oceans*, *118*, 3138–3145, doi:10.1002/jgrc.20236.
Roquet, F., G. Madec, T. J. McDougall, and P. M. Barker (2015), Accurate polynomial expressions for the density and specific volume of seawater using the TEOS-10 standard, *Ocean Modell.*, *90*, 29–43.
Rousset, C., et al. (2015), The Louvain-La-Neuve sea ice model LIM3.6: Global and regional capabilities, *Geosci. Model Dev.*, *8*(10), 2991–3005.
Schaffer, J., R. Timmermann, J. E. Arndt, S. S. Kristensen, C. Mayer, M. Morlighem, and D. Steinhage (2016), A global high-resolution data set of ice sheet topography, cavity geometry and ocean bathymetry, *Earth Syst. Sci. Data*, *8*, 543–557.
Scheduikat, M., and D. J. Olbers (1990), A one-dimensional mixed layer model beneath the Ross Ice Shelf with tidally induced vertical mixing, *Antarct. Sci.*, *2*(01), 29–42.
Schodlok, M. P., D. Menemenlis, and E. J. Rignot (2016), Ice shelf basal melt rates around Antarctica from simulations and observations, *J. Geophys. Res. Oceans*, *121*, 1085–1109, doi:10.1002/2015JC011117.
Schoof, C. (2007), Ice sheet grounding line dynamics: Steady states, stability, and hysteresis, *J. Geophys. Res.*, *112*, F03S28, doi:10.1029/2006JF000664.
Shepherd, A., et al. (2012), A reconciled estimate of ice-sheet mass balance, *Science*, *338*(6111), 1183–1189.
Spence, P., S. M. Griffies, M. H. England, A. M. Hogg, O. A. Saenko, and N. C. Jourdain (2014), Rapid subsurface warming and circulation changes of Antarctic coastal waters by poleward shifting winds, *Geophys. Res. Lett.*, *41*, 4601–4610, doi:10.1002/2014GL060613.
St-Laurent, P., J. M. Klinck, and M. S. Dinniman (2013), On the role of coastal troughs in the circulation of warm Circumpolar Deep Water on Antarctic shelves, *J. Phys. Oceanogr.*, *43*(1), 51–64.
St-Laurent, P., J. M. Klinck, and M. S. Dinniman (2015), Impact of local winter cooling on the melt of Pine Island Glacier, Antarctica. *J. Geophys. Res. Oceans*, *120*, 6718–6732, doi:10.1002/2015JC010709.
Steig, E. J., Q. Ding, D. S. Battisti, and A. Jenkins (2012), Tropical forcing of Circumpolar Deep Water inflow and outlet glacier thinning in the Amundsen Sea Embayment, West Antarctica, *Ann. Glaciol.*, *53*(60), 19–28.
Stern, A. A., M. S. Dinniman, V. Zagorodnov, S. W. Tyler, and D. M. Holland (2013), Intrusion of warm surface water beneath the McMurdo Ice Shelf, Antarctica, *J. Geophys. Res. Oceans*, *118*, 7036–7048, doi:10.1002/2013JC008842.
Stewart, A. L., and A. F. Thompson (2015), Eddy-mediated transport of warm Circumpolar Deep Water across the Antarctic Shelf Break, *Geophys. Res. Lett.*, *42*, 432–440, doi:10.1002/2014GL062281.
Stommel, H. (1982), Is the South Pacific helium-3 plume dynamically active?, *Earth Planet. Sci. Lett.*, *61*(1), 63–67.
Stull, R. B. (2012), *An Introduction to Boundary Layer Meteorology*, vol. 13, Springer, New York.
Thoma, M., A. Jenkins, D. Holland, and S. Jacobs (2008), Modelling circumpolar deep water intrusions on the Amundsen Sea continental shelf, Antarctica, *Geophys. Res. Lett.*, *35*, L18602, doi:10.1029/2008GL034939.
Timmermann, R., and H. H. Hellmer (2013), Southern Ocean warming and increased ice shelf basal melting in the twenty-first and twenty-second centuries based on coupled ice-ocean finite-element modelling, *Ocean Dyn.*, *63*(9–10), 1011–1026.
Timmermann, R., Q. Wang, and H. Hellmer (2012), Ice-shelf basal melting in a global finite-element sea-ice/ice-shelf/ocean model, *Ann. Glaciol.*, *53*(60), 303–314.
Treguier, A. M. (1992), Kinetic energy analysis of an eddy resolving, primitive equation model of the North Atlantic, *J. Geophys. Res.*, *97*(C1), 687–701.
Treguier, A.-M., J. Deshayes, J. Le Sommer, C. Lique, G. Madec, T. Penduff, J.-M. Molines, B. Barnier, R. Bourdalle-Badie, and C. Talandier (2014), Meridional transport of salt in the global ocean from an eddy-resolving model, *Ocean Sci.*, *10*(2), 243–255.
Turner, J., J. C. Comiso, G. J. Marshall, T. A. Lachlan-Cope, T. Bracegirdle, T. Maksym, M. P. Meredith, Z. Wang, and A. Orr (2009), Non-annular atmospheric circulation change induced by stratospheric ozone depletion and its role in the recent increase of Antarctic sea ice extent, *Geophys. Res. Lett.*, *36*, L08502, doi:10.1029/2009GL037524.
Turner, J., T. J. Bracegirdle, T. Phillips, G. J. Marshall, and J. S. Hosking (2013), An initial assessment of Antarctic sea ice extent in the CMIP5 models, *J. Clim.*, *26*(5), 1473–1484.
Wåhlin, A. K., X. Yuan, G. Björk, and C. Nohr (2010), Inflow of Warm Circumpolar Deep Water in the Central Amundsen Shelf, *J. Phys. Oceanogr.*, *40*(6), 1427–1434.
Walker, D. P., M. A. Brandon, A. Jenkins, J. T. Allen, J. A. Dowdeswell, and J. Evans (2007), Oceanic heat transport onto the Amundsen Sea shelf through a submarine glacial trough, *Geophys. Res. Lett.*, *34*, L02602, doi:10.1029/2006GL028154.
Walker, R. T., D. M. Holland, B. R. Parizek, R. B. Alley, S. M. J. Nowicki, and A. Jenkins (2013), Efficient flowline simulations of ice shelf–ocean interactions: Sensitivity studies with a fully coupled model, *J. Phys. Oceanogr.*, *43*(10), 2200–2210.
Weertman, J. (1974), Stability of the junction of an ice sheet and an ice shelf, *J. Glaciol.*, *13*, 3–11.